Tip Induced Quenching Imaging:

Topographic and Optical Resolutions in the Nanometer Range

by

Olaf Schulz

A Dissertation Presented in Partial Fulfillment
of the Requirements of the Degree
Doctor of Philosophy

Approved April 2012 by the
Graduate Supervisory Committee:

Robert Ros, Chair
Marcia Levitus
Stuart Lindsay
Yan Liu
John Shumway

ARIZONA STATE UNIVERSITY

May 2012

ABSTRACT

In this work, atomic force microscopy (AFM) and time resolved confocal fluorescence microscopy are combined to create a microscopy technique which allows for nanometer resolution topographic and fluorescence imaging. This technique can be applied to any sample which can be immobilized on a surface and which can be observed by fluorescence microscopy. Biological problems include small molecular systems, such as membrane receptor clusters, where very high optical resolutions need to be achieved. In materials science, fluorescent nanoparticles or other optically active nanostructures can be investigated using this technique.

In the past decades, multiple techniques have been developed that yield high resolution optical images. Multiple far-field techniques have overcome the diffraction limit and allow fluorescence imaging with resolutions of few tens of nanometers. On the other hand, near-field microscopy, that makes use of optically active structures much smaller than the diffraction limit can give resolutions around ten nanometers with the possibility to collect topographic information from flat samples. The technique presented in this work reaches resolutions in the nanometer range along with topographic information from the sample. DNA origami with fluorophores attached to it was used to show this high resolution. The fluorophores with 21 nm distance could be resolved and their position on the origami determined within 10 nm.

Not only did this work reach a new record in optical resolution in near-field microscopy (5 nm resolution in air and in water), it also gave an insight into the physics that happens between a fluorescent molecule and a dielectric nanostructure, which the AFM tip is. The experiments with silicon tips made a detailed comparison with models possible on the single molecule level, highly resolved in space and time. On the other hand, using silicon nitride and quartz as tip materials showed that effects beyond the established models play a role when the molecule is directly under the AFM tip, where quenching of up to 5 times more efficient than predicted by the model was found.

TABLE OF CONTENTS

page

page

page

CHAPTER

1 INTRODUCTION

1.1 AFM

Atomic force microscopy (AFM) is a technique for imaging the topography and mechanical properties of surfaces, such as stiffness and friction. The first AFM was built in 1985 by Binnig, Quate, and Gerber [1]. An AFM uses a very small cantilever with a pointed probe at its end (compare Figure 1) to probe interaction with the surface, which causes a bending of the cantilever (contact mode) or a change in its mechanical response (AC mode). In modern AFMs, the bending of the cantilever is sensed by reflecting a laser beam off its surface. The laser is detected by a split photodiode. From the differential signal on the different parts of the photodiode, the angle of the reflected beam and thus the bending of the cantilever can be inferred (Figure 2). Typical lengths for cantilevers are around 100 micron in length with spring constants of about 0.001-10 N/m, and deflections below a nanometer can be detected. For imaging, the AFM probe is scanned over the sample while collecting information about the local properties of the sample. For the scanning motion, as well as the movement of the tip perpendicular to the surface, piezo crystals are used. These allow very precise and smooth translocation of the sample and tip, by applying a voltage to them which changes their extension. Although the movement of the piezos can be controlled with below Angstrom accuracy, their precise positioning is influenced by

hysteresis, delayed response (creep) and thermal drift. This is why most piezo stages use capacitors as location feedback. When operated in closed-loop feedback, piezo stages can maintain their position despite thermal drift and be positioned accurately even when exhibiting hysteresis.

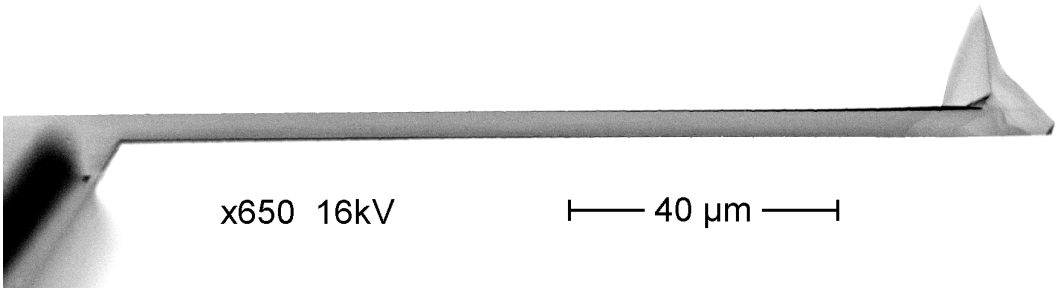

Figure 1
Scanning electron microscope image of an AFM cantilever with tip at the end

As mentioned above, there are two inherently different modes of imaging for the AFM, contact mode and AC mode. In contact mode, the AFM probe is gently pressed onto the surface. Deviations in surface height are detected by a bending of the cantilever. A feedback mechanism changes the height of the AFM probe such that the deflection of the cantilever remains constant. For measurements in ambient conditions, which will constitute the major part of this thesis, one has to take into account strong adhesion forces through capillary interaction between the AFM tip and the surface, which is covered by a layer of water from the air. The height of this layer is in the range of 1 nm and the forces are in the nN range, depending on the chemistry of the surface, whether it is hydrophilic or hydrophobic. This means that the force onto the surface cannot be

controlled accurately below this adhesion force. An effect of this relatively high force between tip and surface is that the tip becomes dull quickly, as it is ground against the surface during the scanning motion. The dull tip has an even higher surface area, which in turn increases the force. Also, high forces make imaging of fragile samples, like biomolecules, impossible. For measurements in liquid this is not a problem, since the AFM probe is completely immersed and no forces from the water boundary act on it.

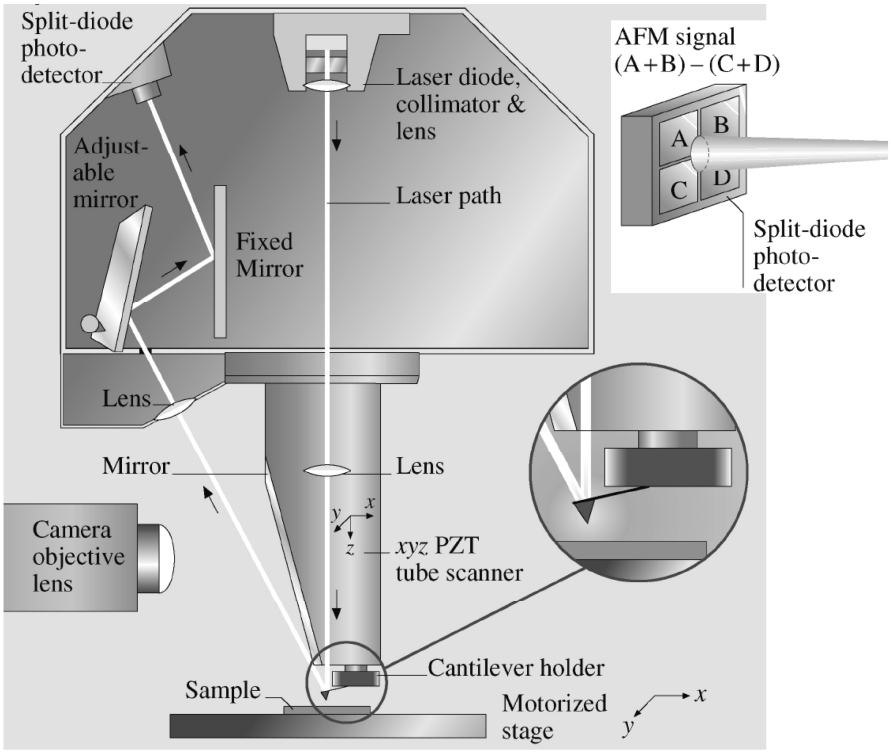

Figure 2

Schematic drawing of an AFM. The cantilever is mounted above the surface. A laser beam is focused onto the cantilever and reflected onto a split photodiode which detects bending of the cantilever. Modified from [2]

In AC mode, oscillations near its resonance frequency are excited in the cantilever. When the probe interacts with the surface, its effective mass changes due to attraction or repulsion from the surface. This alters its resonance frequency and thus the amplitude of the oscillation changes when the exciting frequency is kept fixed. A feedback mechanism keeps the amplitude constant by changing the height of the probe. Typical amplitudes of oscillation are in the range of tens of nanometers, typical frequencies are between 50-500kHz for measurements in air and 5-50kHz for measurements in liquid. Water on the surface is often less of a problem in AC mode, since the probe does not necessarily make mechanical (repulsive) contact with the surface and the tip does not become dull. An application of AC mode in near-field fluorescence imaging is demodulation of the fluorescence signal with the cantilever oscillation which can be used for signal enhancement and background subtraction. This shall be discussed in detail in section 1.4.2.

It should be mentioned here, that apart from imaging, the AFM can also be used to push and pull on structures, like whole cells or single molecules, to determine parameters like binding forces or elastic behavior [3, 4]

1.2 Fluorescence Microscopy

1.2.1 General fluorescence

Fluorescence microscopy is a very widely used technique in the field of life sciences [5-7]. It is, for example, employed to visualize functional elements of

living cells and to study dynamics, structure and transport in living systems, spanning the size range from tissues to single molecules. The ability of fluorescence microscopy to identify particular single molecules makes it an excellent tool for the study of molecular processes like transcription of DNA and translation to proteins and regulatory pathways.

The physical mechanism underlying fluorescence is the excitation of a molecule by means of light into a higher energetic state and the subsequent relaxation of the molecule which is accompanied by the emission of a photon. Because some of the original energy is lost in the molecule's environment, the incident photon and the fluorescence photon have a different frequency and thus color. This can be used to separate excitation and emission light, which is the basis for single molecule sensitivity. [8]

The Jablonski Diagram (Figure 3) helps us understand the processes involved in the fluorescence of organic molecules. At room temperature, the fluorophore is very likely to be in its ground state. When a photon is absorbed, the molecule is transitioned into one of the sub-levels (vibrational states) of the first excited state. This process occurs within about 10^{-15} sec. From there it relaxes to the lowest sub-level of the first excited state within approximately 10^{-12} sec. Now, the fluorophore can be de-excited to one of the sub-levels of the electronic ground state and emit the excess energy as a fluorescence photon. The time in the excited state is on the order of 10^{-9} sec. Finally, the molecule relaxes to the lowest sub-level of the ground state. Because energy is "lost" in the relaxation of the

molecule both in the excited state upon absorption and in the ground state after fluorescing, the energy of the fluorescence photon is generally lower than that of the absorbed photon. This shift in energy is called Stokes-Shift, and it is, naturally, connected to a shift in frequency, and thus color.

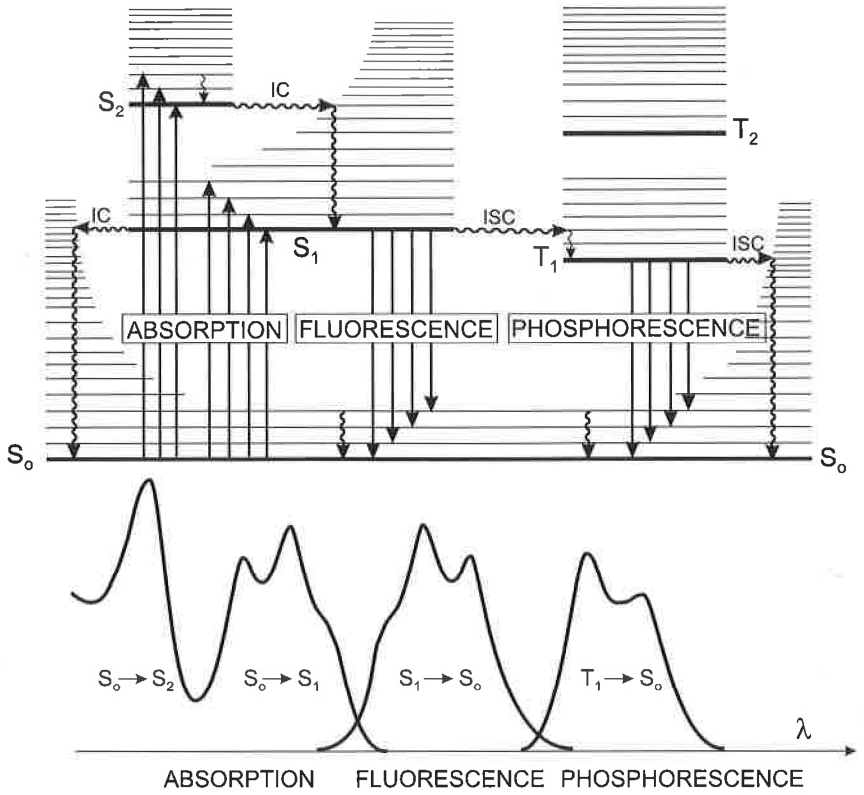

Figure 3

Energy levels of a fluorophore (Jablonski diagram). The electronic states S and T are represented by thick horizontal lines. The vibrational sublevels are indicated as thin horizontal lines. Transitions which absorb or emit a photon are shown as straight vertical lines. Wavy lines indicate radiationless transitions.
The bottom shows the spectra for absorption, fluorescence and phosphorescence. The shapes of the spectra result from the probability of transition into the vibrational levels. From [8]

1.2.2 Fluorescent probes

Important for the applicability of fluorescence microscopy is the availability of stable fluorophores, as fluorescence blinking and bleaching make

investigation at least at the single molecule level difficult [9]. One way to circumvent these problems is by taking the molecule out of the rather complicated aqueous environment and immobilizing it on a surface in air or embedding it in a polymer matrix where interactions between the molecule and its vicinity are minimized. Of course, when one wants to study a biological problem, performing the experiment in a non-aqueous environment is often out of the question. However, imaging of single molecules that are immobilized on a surface in air is often used to study particular aspects of isolated systems. Polymer matrices are often reverted to when one wants to investigate principles of interaction between the fluorophore and an external influence, like an NSOM probe. This will be discussed in detail in section 1.4.

Another type of commonly used fluorophores are semiconductor quantum dots, which are nano-sized crystals of semiconductor material which have a band gap in the optical range (400-800 nm, 1.55-3.1 eV) [10]. Typically, quantum dots are more stable than organic fluorophores; however, intermittent fluorescence and blinking on all time scales make them unsuitable for many applications. Also their toxicity restricts their use for certain biological experiments. In recent years, the development of non-blinking quantum dots has made progress [11].

1.2.3 Instrumentation

There are different schemes of illumination and detection for fluorescence microscopy. Near-field microscopy shall be discussed in greater detail in a

separate section (1.4). Two widely used basic approaches to far-field microscopy which use different methods for both illumination and detection are wide-field and confocal fluorescence microscopy. Wide-field microscopy describes the illumination of a large area of the sample and imaging of this area onto a CCD camera using a microscope objective. In contrast, in confocal microscopy only a diffraction limited spot of the sample is illuminated through a high numeric aperture objective and the fluorescence is recorded using a point detector like an avalanche photo diode or a photomultiplier tube. To recreate an image, the illuminated area is moved through the sample while recording the fluorescence. Because of the use of point detectors, an advantage of confocal microscopy is that the fluorescence can be monitored on very fast time scales down to few tens of picoseconds. Thus, lifetimes of the excited state of the molecule can be extracted [12]. Because a pinhole is used, light from out-of-focus regions will be excluded from detection. This allows for three dimensional imaging of by taking multiple confocal scans at different focus positions.

1.2.4 Single molecule fluorescence

The fluorescence properties of single molecules can be studies under different aspects, such as the chemical composition of the fluorescent molecule and its influence on absorption and emission properties. Also the influence of the environment surrounding the molecule can be addressed from a chemical point of view. When we want to understand the absorption and emission processes, and

the distribution and dissipation of light and energy from the molecule, we need to consider electrodynamics in media. In this framework, we can treat the excited molecule as a point-dipole emitter, which allows us to calculate observed fluorescence and energy transfer to the environment. These aspects shall be addressed in the following. The description of the basics of molecular fluorescence follows the textbook by Bernard Valeur [8].

Typical organic fluorophores which are used as labels in fluorescence microscopy and spectroscopy are usually carbon ring systems. These molecules possess an extended delocalized π–electron orbital, which has a transition to the antibonding π* orbital at energies which correspond to the frequency of light in or near the visible range. The transition from the ground state to the excited state changes the electronic as well as vibrational state of the molecule. In a quantum mechanical description this looks as follows.

$$\left|\left\langle \Psi_1 \chi_a \left| M \right| \Psi_2 \chi_b \right\rangle\right|^2$$

Ψ_1 and Ψ_2 are the electronic part of the quantum mechanical wavefuntions of the molecule before and after the transition and χ_a and χ_b are the vibrational wavefuntions before and after. M is called the transition moment. It describes the change of the electronic configuration of the molecule during the transition. The vibrational wavefunctions χ are not changed by the transition moment M, thus we can pull them out of the bracket.

$$\left|\left\langle \Psi_1 \left| M \right| \Psi_2 \right\rangle\right|^2 \left|\left\langle \chi_a \left| \chi_b \right\rangle\right|^2$$

The factors $\left|\langle \chi_a | \chi_b \rangle\right|^2$ are the so called Franck-Condon factors. They assign a certain probability to a transition according to the change in vibrational energy of the molecule.

The transition of the molecule from the ground state to the excited state is connected with a certain orientation along the molecule, which means that we can treat the transition moment M as a vector (compare Figure 4). This implies that the transition is stronger for excitation by light of certain polarization. This is used, for example, in rotational FCS [13], where the dynamics of rotation are studied through the change in absorption and fluorescence as the orientation of the molecule changes. The de-excitation of the molecule as fluorescence follows the same rules; hence the light emitted from a single molecule can be described as oscillating point-dipole radiation with the dipole oriented along the transition moment M. We can make use of these effects in determining the orientation of an immobilized molecule. The technique of defocused orientation imaging will be described in section 2.9

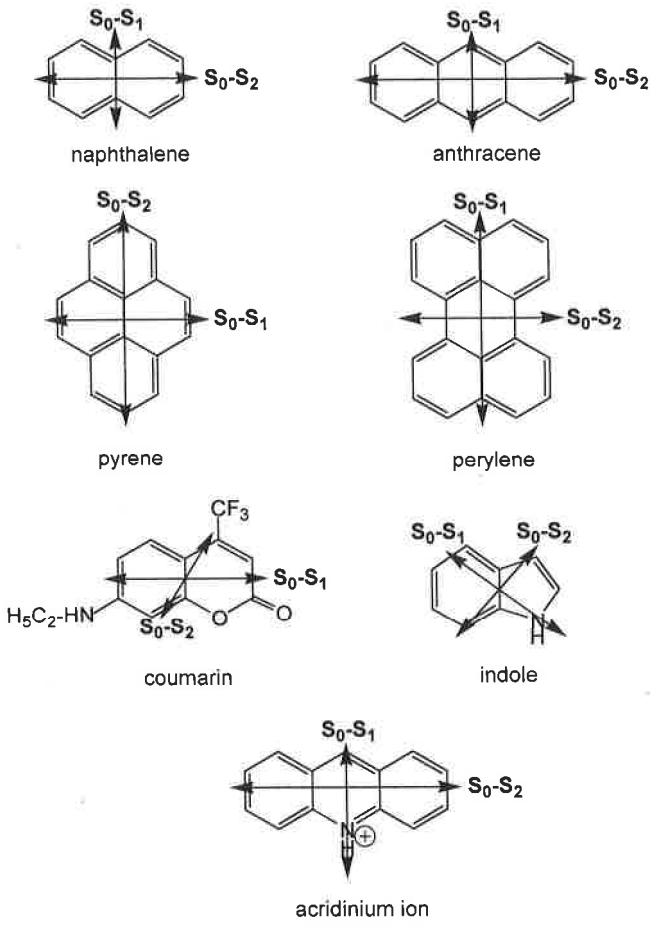

Figure 4

Examples of transition moments for different organic molecules. From [8]

When the molecule makes the transition from the excited state back to the ground state, it can emit a photon or it can release the excess energy otherwise, for example vibration of the molecule (compare Figure 3) or changes of the molecular structure (photoisomerization). These effects concur with fluorescence and lead to a less efficient fluorophore. The efficiency of fluorescence over competing processes is described be the fluorescence quantum yield Q_{fl}. It is the ratio of photons absorbed by the molecule over time and the number of

fluorescence photons. Using the decay rate for radiative processes $k_{r,}$ which are processes that result in the emission of a photon into the far-field, and the decay rate for non-radiative processes k_{nr}, which are any events that lead to the molecule returning to its ground state without emission of a fluorescence photon, we can write the quantum yield as follows

$$Q_{fl} = \frac{k_r}{k_r + k_{nr}}.$$

Another quantity that describes the emission of a fluorophore is the excited state lifetime τ. It is the time between absorption of a photon and return to the ground state. For an ensemble of measurements, the time between absorption and emission of a photon follows Poisson statistics. Thus, after excitation, the fluorescence intensity behaves as $I = I_0 \cdot \exp(\frac{-t}{\tau})$. For organic molecules the lifetime is on the order of a few nanoseconds. For fluorescent quantum dots it is on the order of few tens of nanoseconds.

Besides vibrational relaxation without emitting a photon, the molecule can convert to its triplet state. This means that the spin state of one electron of the molecule changes. In principle this transition would be forbidden quantum mechanically, however, due to spin-orbit coupling, the transition can become possible. The lifetime of the triplet state is usually much longer (microseconds to seconds) than the lifetime for fluorescence. The formation of the triplet state is what leads to intermittent fluorescence emission, called fluorescence blinking. For single molecule experiments blinking usually interferes with the measurement.

However, in techniques like STORM (Stochastic Optical Reconstruction Microscopy) [14] or SOFI (Superresolution Optical Fluctuation Imaging) [15], intermittent fluorescence is used to overcome the diffraction limit and localize fluorophores in dense samples with high accuracy (~20nm) (see section 1.3). Another problem with the formation of the triplet state is that it can be, depending on the chemistry of the molecule, reduced or oxidized to a more reactive state [16]. If the molecule undergoes a chemical reaction before returning to the ground state, the change will likely cause the molecule to lose its fluorescence properties and it cannot be observed any more. This process is called photobleaching. Although photobleaching is usually undesired, it can be used to bleach certain areas of a sample on purpose to study the diffusion of fluorescent molecules into this area [17].

Many experiments in the development of near-field microscopy have been done with fluorophores on surfaces in air or even embedded in polymer matrices. This has the advantage that the fluorescence is much more stable than in aqueous environments. In water, protonation of the fluorophore as well as reaction with oxygen radicals can more easily occur than in air. In polymer matrices, where the fluorophore is protected from a reactive environment, the fluorescence is very stable which makes it a perfect environment to study probe fluorophore interactions in near field optics. The clear disadvantage is, though, that the probe always has a minimum separation from the fluorophore and very short range effects cannot be studied.

Apart from photobleaching the fluorophore can be involved in other photoinduced reactions. The excited molecule has a different wave function than the ground state. This implies that the molecule has a different electronic configuration and thus a different reactivity. A special case is the formation of so called excimers, which are multimers of excited molecules [18].

The photochemistry of fluorophores and particularly the blinking and bleaching behavior of fluorophores in aqueous solutions have been studied by the groups of Tinnefeld and Sauer [16]. They found a way to reduce bleaching and blinking not by preventing the molecule from entering into its triplet state, but by depopulating the triplet state more quickly by allowing reactions that lead back to the ground state. Until then, reducing agents had been used to bring photoionized fluorophores back to the ground state and to reduce the presence of oxygen radicals. This strategy does not work for every kind of fluorophore and sometimes photobleaching becomes even more prominent [19-21]. In their approach they use both reducing agents as well as oxidizers. This opens reactive pathways from the triplet states to either anionic (reduction) or cationic (oxidation) forms of the fluorophore and from there to the ground state by another oxidation or reduction step. In this fashion, the ground state is quickly repopulated and the data shows that blinking as well as bleaching is dramatically reduced.

The spatial distribution of emission from a molecule can be calculated from electrodynamic theory considering the boundaries [22], for example a glass slide onto which a molecule is immobilized. For a molecule in a homogenous

medium, we can use Maxwell's equations to find the distribution of the fields generated. We define an oscillating point dipole as an alternating current in direction $\vec{p}$ and confined to one point in space by using the Dirac delta function. The current density from this dipole is then

$$j = -i\omega \cdot \vec{p} \cdot \delta(\vec{r}) \cdot \exp(-i\omega t).$$

The spatial distribution of the resulting electric field is (in CGS units)

$$\vec{E}(r) = \left[\left(-1 - \frac{3i}{kr} + \frac{3}{(kr)^2} \right) \vec{n}(\vec{n} \cdot \vec{p}) + \left(1 + \frac{i}{kr} - \frac{1}{(kr)^2} \right) \vec{p} \right] \frac{k^2 \cdot \exp(ikr)}{r}, \qquad \textbf{(1)}$$

where k is the wavevector $k = \frac{\omega}{c}$ and $\vec{n}$ is the unit vector in direction of r, and a time dependent part $\exp(i\omega t)$ was omitted. In the near-field zone, $r << \lambda$ or $kr << 1$, this becomes $\vec{E}(r) = \left(3\vec{n}(\vec{n} \cdot \vec{p}) - \vec{p}\right) \frac{1}{r^3}$.

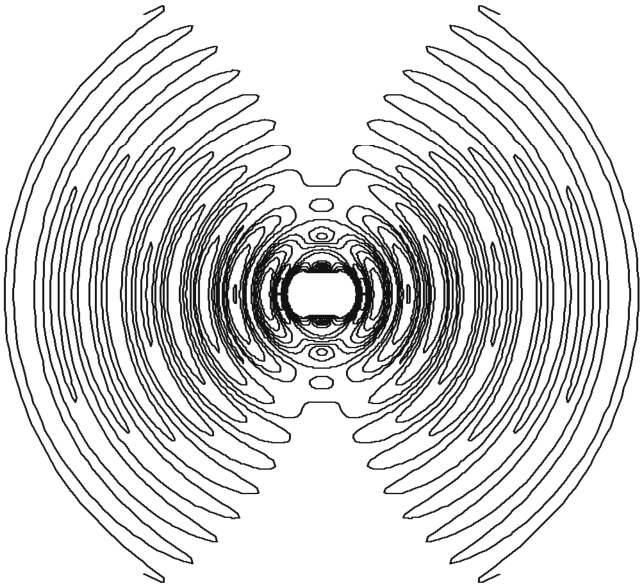

Figure 5

Contours of constant electric field amplitude $\left|\vec{E}(r)\right|$ for a vertically oriented dipole in free space. From [22]

The radiated power can be calculated from the Poynting vector *S*. For the angular distribution of the radiated power we get (in spherical coordinates)

$$\frac{d^2S}{\sin\theta d\theta d\phi} = \frac{cnk^4p^2}{8\pi}\sin^2\theta,$$

which is a donut-shape with no power radiated in the direction of the dipole (Figure 6). *C* and *n* are the speed of light and the refractive index of the medium.

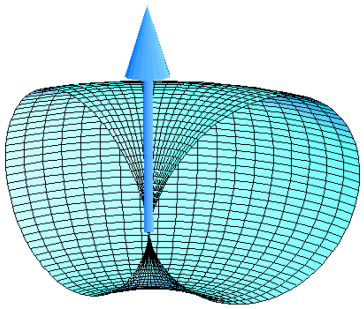

Figure 6
Distribution of radiated power for a vertical dipole in a homogenous medium. From [22]

For the emission of a dipole near an interface between two media with different indices of refraction, we can consider the behavior of plane waves at a planar boundary between two media. The boundary conditions for an incoming, reflected, and transmitted wave give us the amplitudes and phases of the electric fields in both media depending on the polarization of the incoming wave.

Using the expression for the electric field of the radiating dipole in a homogenous medium (equation 1), we can calculate the spatial distribution of emission. It is interesting to see, that, when we calculate the transmitted power

into each medium, the emission into the medium of higher refractive index is favored, leading to another advantage of imaging molecules on surfaces, because much of the radiated power is transmitted to the glass (n=1.5) rather than the upper medium (water, n=1.33 or air, n=1).

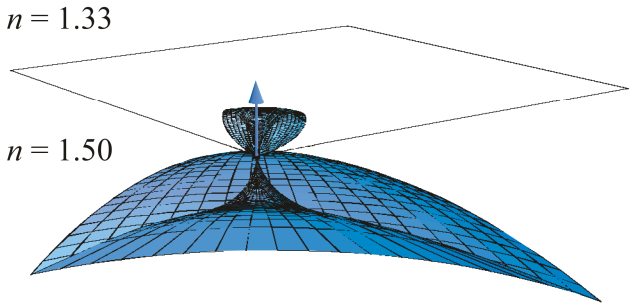

Figure 7
Distribution of radiated power for a vertically oriented dipole on a glass/water interface. From [22]

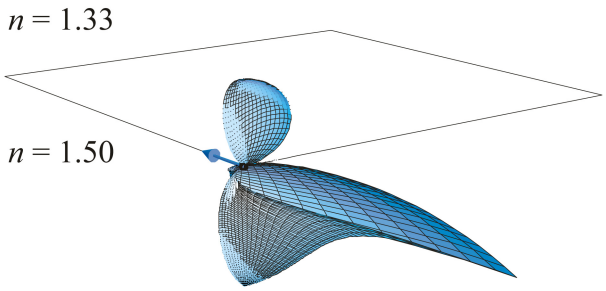

Figure 8
Distribution of radiated power for a dipole oriented parallel to a glass/water interface. From [22]

The emitting molecule is not a continuously radiating dipole source, and we have to consider the semi-classical quantum-mechanical analogies for the results above. As described earlier, a single molecule gets excited by the incident

light into a higher energetic state. Here it stays for a few nanoseconds until it decays to the ground state, possibly emitting a photon. In the case that more power is emitted by the molecule, this must mean that it emits more photons, which translates into a shorter time spent in the excited state before emitting, which would be measured as a shorter fluorescence lifetime. This situation is called radiative enhancement, or enhancement of the radiative rate. In the case where the medium absorbs radiation at the wavelength of emission, which can be described by an imaginary part of the refractive index, we get a de-excitation of the molecule without emission of radiation into the far-field. In this case we speak of non-radiative energy transfer. Since power is transferred into the material this way, the lifetime of the molecule will also be shorter, but in this case resulting in the detection of fewer photons.

Energy can also be transferred to another acceptor of energy, like another fluorophore. The energy can either be transferred electromagnetically in the near-field (resonant energy transfer) [23], or via direct exchange of an electron [24].

Another factor influencing the fluorescence of organic fluorophores is the pressure of the surrounding medium. In the context of near-field microscopy with AFM in contact mode this becomes relevant since the AFM probe can exert very high pressures onto the surface. Experimentally, a red-shift of the fluorescence of organic molecules in solids has been found. In 1968 Peter Jones compared the shift in frequency of the fluorescence of anthracene and tetracene in different host crystals [25]. For all materials, he finds a reversible shift in frequency which

depends linearly on the applied pressure. The shifts are as high as $2.4 \cdot 10^{13}$ Hz/GPa. This corresponds to a shift in wavelength from 650 nm to 686 nm for a pressure increase of 1 GPa. The red-shifts can be explained by a mixing of energy levels of the fluorophore and the molecules in its environment. The calculations are based on a second-order perturbation theory using a dipole approximation for the potentials [26]. Later, when advances in single molecule spectroscopy allowed to monitor smaller changes in frequency, similar results with pentacene in a p-terphenyl host matrix were found by Croci et al. for lower pressures [27].

Irreversible effects onto the emission of pure fluorophore crystals were found by Jones and Nicol [28, 29]. These changes are attributed to the formation of excimers at high pressures.

1.3 Far-field based high resolution fluorescence techniques

All optical microscopy has a limit in terms of resolution. When we focus a beam of light, or image a point-emitter (fluorescent molecule) we are restricted to a certain spatial angle, given by the optics that are being used. In terms of Fourier optics this means that we only get a part of the spatial frequencies and thus a point emitter seems blurred out. This limitation in optical microscopy is called diffraction limit. It is about half the wavelength of the light that is being used, which is approximately 200-300 nm for visible light. As a theoretical limit of the resolving power of a microscope, this has first been predicted by Ernst Abbe in

1873. There are now many approaches to overcome the diffraction limit in fluorescence microscopy that go by the general name of super-resolution fluorescence microscopy (reviews in [30, 31]). In this work, we shall dwell a bit on those approaches which are currently being widely used or under constant development and therefore interesting from an application point-of-view.

In 1994, Stefan Hell developed a technique called STED microscopy (STimulated Emission Depletion) [32], where imaging beyond the diffraction limit is achieved by means of sophisticated optics. Two carefully aligned laser beams are used in STED. First, a beam with the typical Gaussian profile is used to excite the fluorophores in a sample. Then a second donut-shaped beam is used to de-excite all but the fluorophores in the center of the beam. Thus, only molecules in a small region of the sample are excited and their fluorescence emission can be recorded by a point detector. STED is a scanning technique and the image is created by moving the beams through the sample while recording the fluorescence. STED has been applied to high speed imaging and 3D live cell imaging [33].

Another technique on which many others are based uses the fact that the emission of a point emitter produces a certain pattern when imaged. This pattern can be described by a Bessel function and it has been shown that it can be sufficiently approximated by a 2D Gaussian. When only one point emitter is present, a Gaussian can be fit to its emission profile and the center of the fitted function coincides with the location of the emitter. This technique is called

FIONA (Fluorescence Imaging with One Nanometer Accuracy) or super-accuracy, and as the name suggests, the location of an emitter can be determined with an accuracy in the nanometer range, depending on the quality of the fit, which depends on the number of photons observed [34-36].

Naturally, the emitters in a given sample are usually denser than a few hundred nanometer apart, and FIONA by itself is not applicable any more. Several methods have been developed that are based on the idea that at a given time, only a small subset of possible emitters is actually in a state where they can emit photons. If the members of this subset are separated enough, Gaussians can be fit to their emission patterns and their positions determined. Over time, all emitters will have contributed to the signal and an image with their positions can be created.

This method is realized in different ways. At about the same time, PALM [37] and STORM [14] were developed. PALM, which stands for Photo Activated Localization Microscopy, makes use of certain fluorescent proteins that can be brought into a fluorescent state by photo-activation. Since only a small subset of proteins is activated at a time, FIONA can be applied. STORM (Stochastic Optical Reconstruction Microscopy) uses the fact that fluorescent molecule usually have “dark” states, in which they do not emit photons (blinking). Again, when most molecules are in the dark state, the position of the remaining emitters can be determined using FIONA. Another variant of this scheme is d-STORM (direct-STORM) [38], where the dark state of the fluorophore is induced by

means of photo-deactivation, and –reactivation. By adjusting the intensities of the reactivating light, the number of active fluorophores can be directly controlled.

Another approach to super-resolution microscopy makes use of the fluctuations of individual emitters. In SOFI (Superresolution Optical Fluctuation Imaging) [15, 39], the inherent flickering of single molecule emitters is used to determine their position more precisely than the diffraction limit allows. When the emission pattern of a fluorophore is spread over multiple pixels on a detector, a correlation between neighboring pixels can reveal the center of the emission.

All techniques mentioned above increase the resolution to about 20 nm. Theoretically, super-accuracy can reach resolutions of 1 nm, practically, this has not been achieved.

1.4 Near-field optics

1.4.1 Fluorescence modulation near surfaces

The fluorescence of a single emitter changes as its distance or orientation to a surface are changed. Both the fluorescence intensity and the fluorescence lifetime are affected. Also the spatial distribution of the radiation emitted from the fluorophore can be changed. In the late 1960s, Drexhage and co-workers undertook several experiments where a layer of dye molecules is separated from a flat metal surface by means of Langmuir-Blodgett films, and the fluorescence lifetime and intensity are measured [40]. Because different samples need to be compared to get the distance dependence, the fluorescence lifetime is used as a

measure for the interaction, since the fluorescence intensity may vary over multiple experiments for technical reasons. In 1978, Chance, Prock, and Silbey published a model which explains the behavior of the fluorescence [41]. Their starting point is a driven oscillating dipole. The driving force is the electric field from the incident light and from the light reflected by the surface. The model predicts oscillations of the fluorescence lifetime with the distance of the fluorophore from the metal surface. The dependence is different for molecules with their transition dipole oriented parallel or perpendicular to the surface. For an isotropic mixture of orientations, the model matches the experimental data well.

In the 1980s, similar experiments were performed with dielectric surfaces. Instead of Langmuir-Blodgett films, LiF and SiO spacers were used to separate the fluorophores from silicon and GaAs surfaces [42-45]. In 2007 and 2012, Danos et al. published experiments where they used Langmuir-Blodgett films of different thickness on the same sample to separate fluorophores from a silicon wafer. In this configuration, they were able to compare fluorescence intensities, and show effective fluorescence quenching for small separations of fluorophore and silicon (about 80% quenching for 2nm separation) [46, 47]. Deviations from basic dipole-mirror interactions for small separations were found experimentally [42, 48], and explained theoretically [49].

The orientation dependence of the fluorescence modulation can be visualized by taking a dipole in front of well reflecting surface and using the method of image charges [50]. In case the dipole is oriented parallel to the

surface, its mirror image is oppositely oriented (Figure 9)

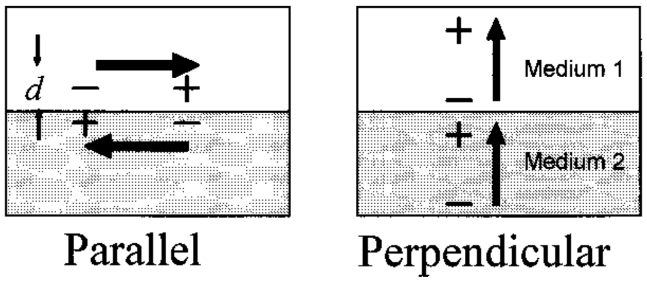

Figure 9
Illustration of the effect of dipole orientation onto the fluorescence emission. When the dipole is parallel to the surface, its mirror image is oppositely oriented (left). When the dipole is perpendicular to the surface, it is oriented the same way as its mirror image. From [50]

For an oscillating dipole this would mean that the dipole and its mirror image oscillate out-of-phase, which results in less emission from the combined system. For a dipole oriented perpendicular to the surface, the mirror image will be oriented in the same direction and the dipoles oscillate in phase, which leads to stronger emission. Further away from the surface, the intensity oscillates due to the change in phase between the dipole emitter and its mirror image.

Figure **10** shows the distance dependence of the fluorescence decay rate.

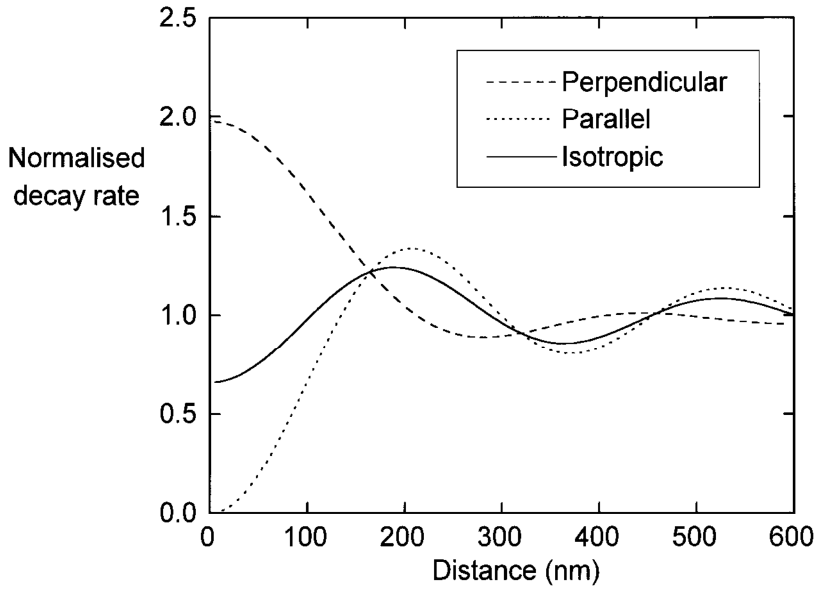

Figure 10
Normalized decay rate (fluorescence intensity) of point emitters of different orientation in front of a silver mirror. From [50]

1.4.2 Near-field microscopy

One way to achieve optical super-resolution is near field microscopy (reviews in [51-53]). This means that the light interacts with structures that are smaller than its wavelength. By scanning over a sample, these interactions can be monitored and formed into an image. There are two inherently different methods in scanning near-field optical microscopy (SNOM[1]). On the on hand, one can make use of a sub-wavelength aperture from which excitation light emanates or through which the emission from the sample is detected, or both. On the other hand, one can probe highly localized interactions of excitation and emission

[1] Two acronyms, SNOM and NSOM, are being used.

photons with a sub-wavelength structure, usually in the size range of few tens of nanometers down to few nanometers. This is usually referred to as apertureless NSOM, or aNSOM.[54]

NSOM and aNSOM both require the sample to be on a surface above which the probe can be placed. Two mechanisms of distance control are employed. For aperture NSOM and aNSOM, both shear force feedback of a horizontally oscillating probe [55] as well as cantilever based probes [1] are employed. In the case of the use of cantilevers, both contact mode and AC mode are applied, but AC mode is more common, since it leaves the probe sharp and provides a natural means for signal enhancement and background subtraction [56]. Contact mode, however might provide higher spatial resolutions and the application of the technique to imaging in liquid would be straightforward.

In case the tip is oscillated vertically above a fluorophore on the sample surface, its influence onto the fluorescence changes constantly. Depending on the polarization of the exciting light, the orientation of the fluorophore, and the material and geometry of the AFM tip, enhancement and quenching of the fluorescence can occur. When the fluorescence signal is correlated with the oscillation of the fluorescence, the signal from only a certain height of the tip above the sample can be chosen where the influence of the tip is most prominent. This means that the fluorescence influenced in the near field of the tip can be separated from the “background” which is, in this case, the unmodulated fluorescence. This leads to high contrast in images created with this data.

Practically, a lock-in amplifier is used to demodulate the fluorescence signal at the oscillation frequency of the AFM cantilever. By choosing the phase of the signal, the near-field zone can be selected. Figure 11 illustrates the method in the case of fluorescence enhancement. The enhancement from the tip is highly localized and superimposed with the normal emission profile from the molecule.

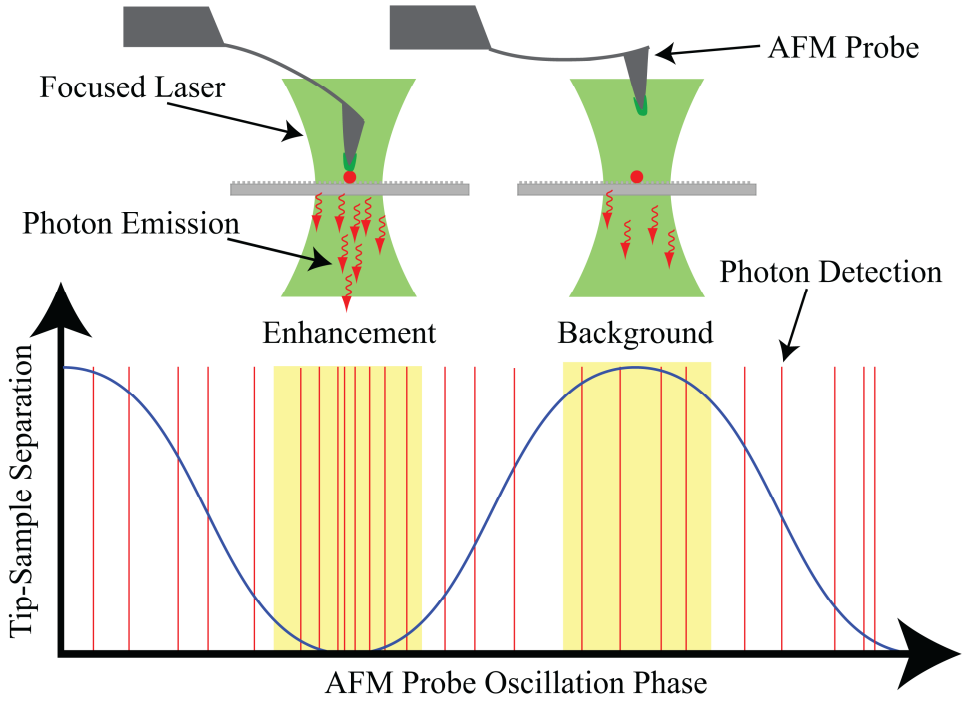

Figure 11

Illustration of fluorescence enhancement in AC mode. When the tip is at a certain phase of its oscillation, more fluorescence is detected. The fluorescence signal can be separated by phase of the oscillation to pick out fluorescence enhancement.

1.4.2.1 Aperture NSOM

The idea to use subwavelength apertures to overcome the diffraction limit in optical imaging was first published by Synge in 1928 [57]. The concept could not be realized at that time because of the lack of sufficient micro- and

nanofabrication techniques. The first experimental realizations with visible light were published by Pohl [58] and Lewis [59] in 1984.

A common approach to create sub-wavelength apertures is by using optical fibers [53]. The fiber is either pulled or etched to leave a pointed end which is coated by a thin (~50-100nm) layer of metal, usually aluminum, to make it opaque. The end of this tip is then opened, for example by focused ion beam, to leave an opening in the aluminum coating through which light can penetrate. The thusly created aperture is around 50-150 nm in diameter. Because the aperture is much smaller than the wavelength of light in the visible region of the spectrum, the light does not penetrate as radiation, but rather as an evanescent wave. This has the consequence that the throughput of the fiber is relatively small (10^{-4} – 10^{-7}) [53]. Much of the original excitation power goes into heating of the fiber, which proves problematic and restricts the power output of the fiber.

A feature of aperture NSOM is that the aperture is not only a passive opening for the light, but the metal coating interacts with the radiation and the fluorophores. Depending on the polarization of the light and the orientation of the fluorophore's transition dipole, enhancement or quenching of fluorescence can be observed. The electric field generated by the excitation light is not uniform, thus distinct patterns arise in the image. From these patterns, the orientation of the transition dipole moment of the molecule can be inferred [60, 61]. Because the fiber probes are relatively large though, these patterns are usually not smaller than 50nm [62].

The mechanisms that allow for distance control in NSOM also give direct access to topographic information of the sample surface. However, since the aperture probes are rather large and the grainy texture of the aluminum coating is not reproducible, good quality topography imaging with these probes is problematic. [51]

A hybrid between aperture NSOM and aNSOM is the tip on aperture (TOA) approach. Here, a nanosized tip is grown on the edge of a subwavelength aperture. This method directly reduces far-field background, since the illuminated area is restricted by the aperture size. Another advantage is that the tip can collect topographical information from the sample with higher accuracy and reproducibility than regular aperture NSOM. Frey et al. used the TOA approach with a metallic tip[2] to achieve an optical resolution of 25 nm [63]. Later, the group used the same technique to image Cy3 labeled DNA. They achieve good resolution in the topographic and optical image. Also they were able to determine the orientation of the fluorophore's transition dipole moment from the pattern created by the interaction between tip and fluorophore [60]. Taminiau et al. measured the change in the spatial distribution of the emission of single fluorophores in the proximity of a metal tip by observing the change in polarization of the emission from the fluorophore [64].

[2] The probe was produced by growing a carbon tip onto the aperture and evaporating aluminum onto the tip at a 45 degree angle. The carbon tip is grown in an electron beam, where trace impurities from the vacuum build up on the surface.

1.4.2.2 Apertureless NSOM

In the past years the combination of AFM and fluorescence has been pushed towards high resolution optical imaging mainly by two research groups. The work of Uri Banin focuses on high resolution imaging of luminescent nanoparticles. The group of Jordan Gerton has been able to achieve optical resolutions below 10 nm (FWHM[3]) in combined images of organic fluorophores

In 2006 Ebenstein et al. have published work that compares the influence of metal coated and dielectric AFM probes onto the luminescence of semiconductor nanocrystal quantum dots [65]. They measured fluorescence intensity as well as lifetime and compare their findings with a simple model of a dipole emitter in front of a planar surface. In their work, they use contact mode AFM as well as AC mode AFM. For the measurements in contact mode, the quatum dots are embedded in a about 10 nm thick layer of PMMA (Polymethylmetacrylate) to prevent them from being swept away by the AFM probe. For measurements in AC mode this is not necessary and thus the sample topography can be recorded as well. The optical setup of the experiment is confocal using circularly polarized light. In this arrangement the light above the sample surface is mainly polarized parallel to the surface, thus, quenching due to dipole-dipole interaction should occur. The sample remains fixed in the confocal volume during the experiment and the AFM tip is scanned over it.

[3] Full Width at Half Maximum is a means of quantifying the resolvability of neighboring peaks in a signal, originally in spectroscopy (Houston, 1926). It is now a common means to compare the quality of super-resolution techniques.

For contact mode, they find quenching of the fluorescence using platinum coated tips and tips that are functionalized with InAs nanocrystals, which were assumed to act as good energy acceptors for the quantum dots used in the experiment. For unmodified silicon probes, they find no optical contrast in the combined images, which is in contrast to the results presented in this thesis. This could be due to orientations of the molecular transition dipole which do not show strong quenching or enhancement from the silicon. Another explanation could be that the silicon probe remained very sharp during the experiments. In this case the quenching from the tip would be highly localized and could have been lost in the pixilation of the image (presumably about 4nm/pixel) and noise.

Their results for combined AC mode AFM and fluorescence show enhancement as well as quenching for silicon probes. For platinum coated probes they find quenching only. The fluorescence data that is collected is correlated with the oscillation of the AFM tip, so the distance dependence of fluorescence can be plotted. For the quenching due to the silicon and platinum coated tip both, they find very good agreement with electrodynamical calculations of a dipole emitter parallel to a silicon plane. In the case of silicon, the distance dependence for pixels besides the quenched spot shows enhancement for small separations. Their data seems to be consistent with a dipole perpendicular to a silicon plane, but the authors do not show this comparison.

In 2008 the group added fluorescence lifetime measurements to their experiment [66]. The experimental setup and the illumination and detection

scheme are basically the same, only pulsed laser light is used for excitation, and the information about tip oscillation as well as the laser pulse frequency is used to extract fluorescence lifetimes as well as surface separation dependence from the data. Again, the sample used for imaging are CdSe quantum dots with an emission wavelength around 630 nm. As AFM tip material, silicon, as well as platinum coated silicon, were used. For both kinds of tips they see quenching under the AFM probe for small tip – surface separations which goes along with a decrease in fluorescence lifetime. For silicon, the data also shows enhancement besides the tip, which is consistent with their previous findings. The change in fluorescence lifetimes is more localized than the change in fluorescence intensity. Hence, the authors propose to use the lifetime to define the optical resolution of the images. They find spots as small as 16 nm (FWHM). Using the same model as in their previous work, they calculate the change in fluorescence intensity and lifetime for a dipole parallel to a plane surface at different distances. Their data fits the model well. However, they do not take into account the change of orientation of the dipole with respect to the tip surface during a scan.

Recently (2010) the group has conducted experiments, where the access to topographic as well as fluorescence data gives insight into localization of the exciton inside a fluorescent nanorod [67]. The nanorods consist of CdSe cores with an asymmetric CdS shell. The experimental setup is the same as above. The resolution from the lifetime data is 15 nm, which is consistent with their previous results. For smaller core particles (2.2 nm) the quenching experiments delivered

no results, which the authors attribute to the small amount of photons collected from these samples. Hence, they changed the polarization of the exciting laser beam to radial. This creates a strong vertical polarization in a tightly focused spot. A vertical transition dipole under the AFM probe leads to enhancement of the fluorescence. Again, the location of the exciton can be localized within 16 nm.

The group of Stephen Quake, and later the group of his student Jordan Gerton, have reached the highest optical resolutions (below 10 nm, FWHM) in the combination of AFM and fluorescence microscopy. In 2004 Quake and Gerton published their first single molecule paper where they are able to collect highly localized fluorescence data at an enhanced signal to noise ratio [68]. The experimental setup consists of a commercial AFM (Bioscope, Digital Instruments) with a silicon tip and a confocal fluorescence microscope. The excitation light is shaped by a beam mask such that only on edge of the laser beam reaches the microscope objective. This leads to a focused evanescent field above the sample surface with a strong polarization vertical to sample surface [69]. The AFM is operated in AC mode with oscillations of 30-40 nm amplitude with the tip being in contact at the lowest point of the oscillation. Using silicon tips, they find fluorescence enhancements of up to a factor of 20. Correlation between the fluorescence intensity and the cantilever oscillation yields the separation dependence of the fluorescence. For spherical CdSe-ZnS quantum dots, the distance dependence shows a very small half maximum of 1.7 nm, which leads to a lateral FWHM of the fluorescence signal of 8 nm. It should be mentioned here

that this resolution is the maximum of a distribution of spot sizes. The smallest spot sizes are 2 nm, which is only one pixel. This leads to the question whether blinking or bleaching affect the measurement; if the fluorescence is interrupted while scanning the molecule, the spot in the resulting near-field image would appear smaller.

In 2006 the group published similar work, but with individual organic dye molecules (Cy3) and Cy3 attached to double stranded DNA of 60 bp length [70]. For the individual molecules, they find spot sizes of about 7 nm, which corresponds to the results with quantum dots. With the DNA-linked Cy3 molecules, they show true resolution of two neighboring point emitters. They find an average distance of the two molecules of 13 nm +/- 4.1 nm, which is, within the error, consistent with the helical rise of double stranded DNA as determined from x-ray structures.

In the same year, Gerton and his group published tip enhanced fluorescence microscopy data from high density samples [71], and in a publication in 2008 [72], they estimate a maximum density at which individual fluorophores are still resolvable. This is particularly relevant for this thesis because the application of quenching microscopy in contact mode AFM is inherently limited to a few molecules within the diffraction limited spot since the

quenching signal becomes weaker as more emitters are present[4]. In their work they find that for ideal experimental conditions, namely a fluorescence enhancement factor of about 20 und radial polarization, the density is only limited by the resolution, which means that all fluorophores must be at least about 10 nm apart from each other.

Also in 2008, the group conducted experiments with carbon nanotube tips [73]. The advantage of using carbon nanotubes for AFM imaging is their high aspect ratio and small size. However, the spot sizes in their combined images were not smaller than 20 nm with nanotubes of about 10 nm diameter. In detail, they measured the influence of the carbon nanotube onto the fluorescence of quantum dots. The illumination scheme was either focused radially polarized light or a beam shaping mask was used as before. Although the carbon nanotubes used should have been a mixture of metallic and semiconducting tips, thus enhancement as well as quenching should have been observed for both kinds of probes, they found quenching only.

Many apertureless scanning near-field optical experiments have been carried out with metal coated tips [74], full metal probes [75], or tips modified with metallic nanostructures [76]. The use of metals with frequencies in the optical range allows for coupling between an emitter and surface plasmons in the metal. In the case of structured tips, the structures have been chosen to have

[4] For n emitters in the diffraction limited spot, the quenching signal is N_0, where N_0 is the number of photons from each emitter, which is for simplicity assumed to be the same. This gives a signal to noise ratio SNR(n) of $\frac{N_0}{\sqrt{n \cdot N_0}} = \frac{1}{\sqrt{n}} \mathrm{SNR}(1)$.

electronic resonances at frequencies of the optical transition of the fluorophore or the frequency of the exciting light. The coupling to surface plasmons in the probe can lead to very strong enhancements. For gold bow-tie structures, enhancement factors of more than 10000 have been shown experimentally [77]. All these techniques achieve super-resolution in the sense that they give spot sizes smaller than diffraction limit, however, because of the size of the nanostructures, which is usually several tens of nanometers, spot sizes below 20 nm could not be reached.

A qualitative analysis of the dependence of the distance between metal structures and fluorophores onto their emission properties has been achieved by means of aNSOM. Kuehn et al. [78] used a single gold nanoparticle attached to a glass probe for enhancement of single molecule fluorescence and compared their results to electrodynamic calculations [79].

aNSOM has also been applied to imaging in liquid. Hoeppener et al. showed resolutions in the optical image of 50 nm [80, 81]. They imaged fluorophore labeled membrane proteins from cells immobilized on a glass substrate and subsequently torn open such that a flat membrane sample remains on the surface. The resolution of the near-field image allows clear distinction of individual proteins in the membrane.

Frey et al. used a cantilever based approach to image single molecules in aqueous environment [82]. The cantilever oscillated vertically, which allows for distance dependent demodulation of the fluorescence signal. They show resolutions of 15 nm and signal-to-noise ratios of up to 76 in the near-field image.

1.4.2.3 Computer modeling of near-field interactions

Above, theoretical models that describe the behavior of emitters near interfaces have been described. To model the influence of a near-field probe more accurately one needs to take into account the geometry of the probe. There are multiple approaches to modeling such systems. When the geometry is approximated with simple structures (like a sphere), the model can be solved analytically [83]. If a more realistic geometry is needed, two different techniques can be used. In *Finite Difference Time Domain* (FDTD), the space is broken up into elements and time is discretized. After each time step, electric and magnetic fields are calculated on the corners and faces of the spatial elements. For the simulation of near-field experiments this technique is problematic, since rather large geometries (microns) with very small elements (nanometers) are needed, which makes it computationally expensive. Also, the presence of point-dipole emitters is problematic in FDTD [84]. Another approach is the *Multiple Multipole* Method (MMP) [85]. Here, the electromagnetic response of a structure (e.g. near-field probe) is approximated by a multipole expansion where the multipoles are positioned near the structure according to its geometry. For each medium, inside and outside the structure, the multipoles are positioned along the boundary to the adjacent medium. To avoid singularities, they are place inside the adjacent medium (Figure 12).

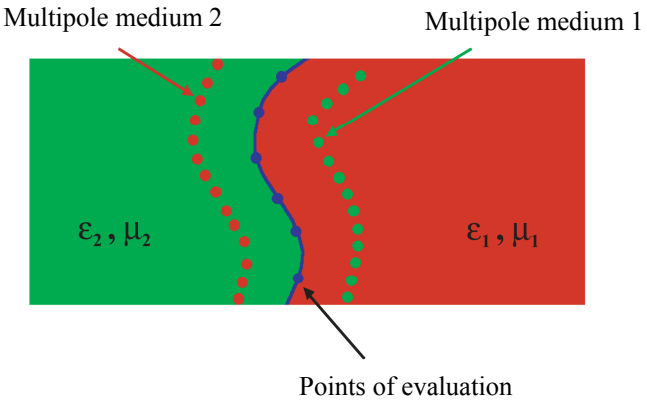

Figure 12
Distribution of multipoles near a boundary between two media with different permeability and susceptibility. The multipoles are placed near the boundary in the adjacent medium. The electric and magnetic fields are evaluated at points on the boundary.

While the MMP method is computationally inexpensive, the placement of the multipoles is critical for a solution for a given geometry, and must be adjusted carefully when the geometry is changed. An application of MMP to near-field microscopy and the comparison with experimental data was published by Novotny and Bharadwaj [86]. They use a gold nanoparticle attached to a glass fibre as near-field probe and find quenching and enhancement of fluorescence of molecules, and the experimental results are compared with MMP calculations.

CHAPTER

2 METHODS AND MATERIALS

2.1 Experimental setup

The experimental setup consists of two commercial microscopes, an Asylum Research MFP-3D Bio AFM and a MicroTime200 confocal fluorescence lifetime microscope from PicoQuant. The sample stage on the microscope body of the MicroTime200 is replaced by the AFM scanning stage, which holds both the sample and the AFM head. The AFM stage consists of two x-y translation stages. The translation stage which holds the sample and allows for rough alignment of the sample with the AFM probe is mounted onto a stage which can move the whole AFM head. This way, the AFM can be moved with respect to the microscope objective underneath.

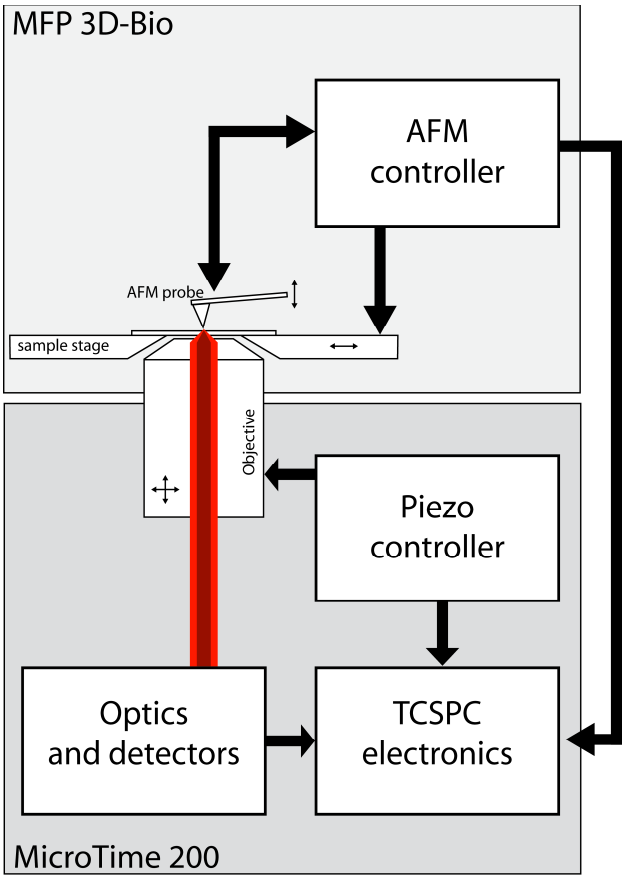

Figure 13

Control, and flow of information in the system. The AFM controller regulates the height of the AFM probe as well as the scanning motion of the piezo scanning stage. Information about the position of the scan stage are fed into the TCSPC electronics, where the signal from the single photon detectors is processed. The objective can be moved by means of a piezo, which is used for alignment. When the optical setup is used without AFM, the objective can be used to scan, in which case information about the movement is fed into the TCSPC electronics.

The MicroTime200 uses time correlated single photon counting (TCSPC) to record fluorescence intensity and lifetime. Pulsed lasers are used for excitation of the fluorophores. When a fluorescence photon is detected, its time difference to the preceding laser pulse is calculated and the information about the arrival time of the photon and the time after the laser pulse are written into a continuous data stream. For imaging, the photon events are sorted into pixels according to their

arrival time using information about the timing of the scan. The two microscopes are synchronized by means of marker signals from the AFM controller, which controls the movement of the sample in a combined scan. At the beginning and end of each scan line, the AFM controller produces a signal which is embedded in the TCSPC data stream. Figure 14 illustrates the synchronization.

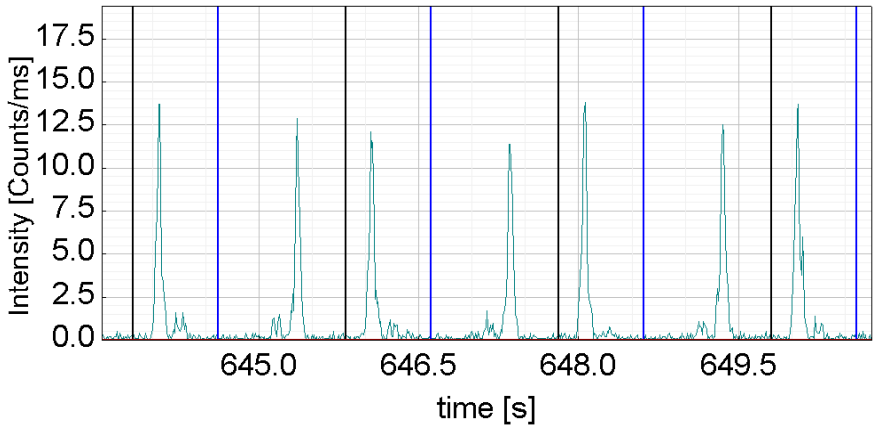

Figure 14

Illustration of the synchronization of AFM and confocal microscope during a combined scan. Into the TCSPC data stream, shown here as the intensity time trace, are embedded marker signals from the AFM controller. The blue and black lines indicate the start and end of a scan line. The AFM scanner makes a continuous back and forth motion during the scan, of which only one direction is recorded. The intensity information from between the start and end marker are sorted into pixels to create a line of the fluorescence intensity image.

An advantage of this method is that the synchronization of the two instruments delivers natural alignment of near-field images recorded by the two microscopes. Because the information displayed in the images is recorded in time, rather than in space, no shifting of the images is needed to align them. The synchronization was adjusted to within about a quarter of a pixel by feeding the marker signals back into the AFM.

While the alignment of the near-field images comes naturally with the synchronization, the AFM probe must still be aligned physically with the confocal volume. This is achieved in two steps. First, by using the lower translation stage, the AFM is moved roughly above the center of the microscope objective. This process is checked by a video camera which collects and live image of the AFM cantilever in a top- down-view. For this, the confocal laser is turned on and the AFM is moved until the laser spot is near where the AFM probe is expected to be. In a second step, the microscope objective is moved by means of piezos until the AFM tip is directly centered in the confocal spot. To monitor the position of the AFM tip in the focus, back-reflected laser light from the sample surface is used. The MicroTime200 has a built in CCD camera for beam diagnostic purposes. It collects the scattered laser light which is reflected by the dichroic, which appears as a symmetric pattern that depends on the polarization and focus of the laser beam. The presence of the AFM probe changes the scattering at the surface (compare Figure 16), thus, when the AFM probe is brought close to the laser focus, this pattern is distorted. The microscope is moved until the pattern is symmetric again which indicated that the AFM tip is centered in the spot. This alignment procedure is fast, requires only very low laser power, which prevents photobleaching, and accurate within about 10 nm. The alignment has been shown to work on glass and on mica surfaces in air and on glass in liquid with various kinds of AFM probes.

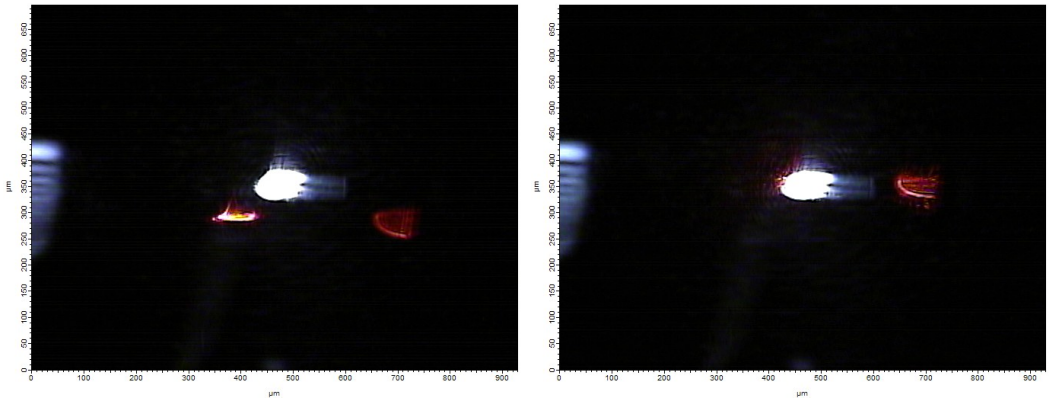

Figure 15

Top-down camera view. The AFM with sample stage can be moved with respect to the microscope objective to roughly align the confocal laser (bright red spot) with the AFM tip. The bright white/blue spot is the reflection of the AFM laser from the cantilever. The weaker spots are reflections inside the optics before the CCD camera.

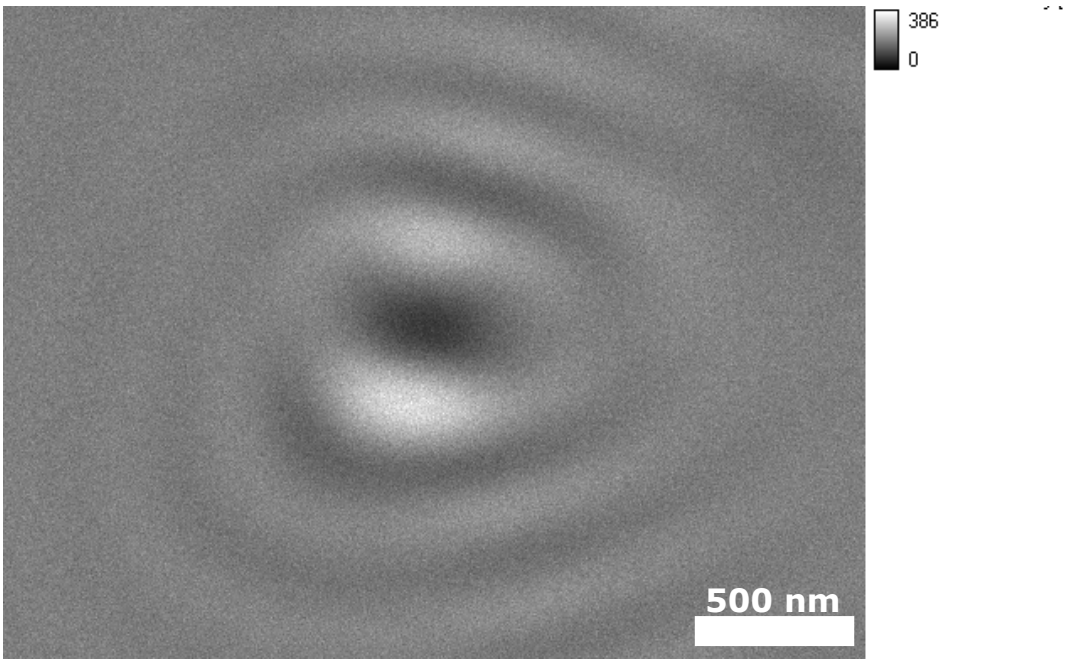

Figure 16

Influence of the AFM probe on scattering from the sample surface. The image shows a confocal scan (objective scan) with low laser power without fluorescence filter. A small fraction of the scattered light passes the dichroic and can be detected. The concentric patterns are due to interference of light reflected from the tip. The scattered light can be used to align the AFM tip and the laser focus.

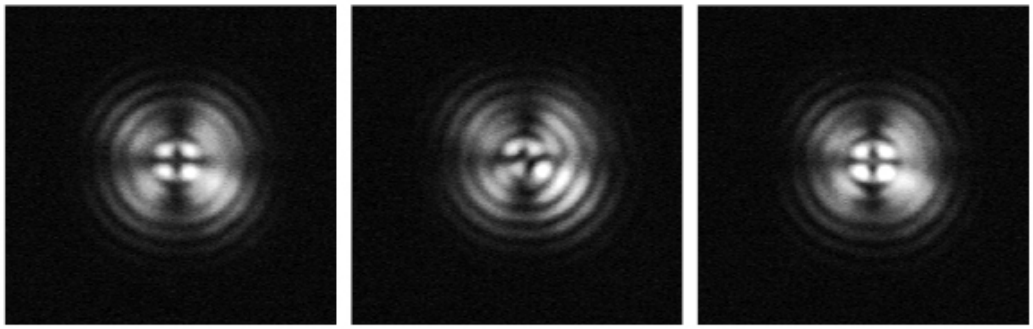

Figure 17

Beam diagnostic camera image. The scattered light from the sample surface is imaged onto a CCD camera, where it appears as a symmetric pattern (left). When the AFM tip is brought into contact with the surface (middle), a distortion of the pattern appears, granted good rough alignment. The objective is then moved until the pattern is symmetric again, with the AFM probe in the center of the objective (right).

2.2 AFM probes

Silicon probes: Point Probe Plus, NHC, from NanoWorld (Switzerland) and Shocon, from AppNano (California)

Silicon nitride probes: SiN probes for soft contact mode, Budget sensors (Bulgaria)

Quartz probes: Prototype Material CB, NanoWorld (Switzerland)

2.3 Chemicals

Water from a MiliQ Synthesis system, Milipore, was used for all cleaning and dilutions. Ethanol was purchased from Koptek (Pennsylvania). Acetone and chloroform was purchased from VWR. Atto dyes were purchased from AttoTec

(Germany). Alexa dyes were purchased from Invitrogen (New York). All other chemicals were purchased from Sigma-Aldrich (Montana).

2.4 Cleaning glass

For the single molecule experiments, VWR coverslides No1 were used after cleaning as follows:

Ultrasonicate in:

- Acetone 5min
- Ethanol 5min
- Water 5min, Milipore water
- blow dry with nitrogen.

The cleaning procedure was performed in a Teflon holder.

2.5 Surface modification

The procedure for silanization is based on references [87, 88].

For imaging in liquid, the fluorophores were immobilized covalently, by binding to amino groups on the surface. The surface was modified with an amino-silane as follows:

After cleaning in solvents (section 2.4),the glass slides were cleaned and hydrophilized in oxygen plasma at high power, for 10min. For plasma cleaning, the slides are put in a glass petri dish on pieces of parafilm.

Incubation in 3-Amino(propyl)triethoxysilane (APTES) or 3-Amino(propyl)trimethoxysilane (APTMS) about 1mM in Chloroform for 40min

After incubation, the glass is ultrasonicated in:

- Chloroform 5min,
- Ethanol 5min,
- Water 5min,
- and finally blown dry with nitrogen.

The incubation in silane and the following cleaning are performed in the same Teflon holder.

2.6 Mica on glass

For experiments with lambda-DNA and DNA origami, transparent samples of thin sheets of mica on glass cover slides were made. The procedure follows Ma et al. [70].

Glass is cleaned according to section 2.4. High grade mica is cut to a size of about 1cm x 1cm. Using Scotch tape, the mica is cleaved until the surface seems smooth and shows little or no boundaries. Then Scotch tape is attached to one edge of the piece of mica and pulled off. This procedure can result in very thin pieces of mica attached to the tape. This thin mica sheet is then cut off from

the tape and placed onto the cover slide. Adhesive forces[5] lead to a strong bond between glass and mica. For incubation with liquids, the edges of mica must be sealed. This is achieved by masking the sample with Kapton tape (Kapton brand, 50mil).

2.7 DNA

lambda-DNA at a concentration of 458 µg/ml was purchased from Promega. The DNA was diluted 1:100 in Tris buffer containing 5mM nickel chloride [89], and stained with YOYO-1 (Invitrogen) at a concentration of about 1:4 (fluorophore : base pair). For sample preparation, a few µl of solution were put on a piece of mica on glass (section 2.6), and incubated for 1 min, then rinsed with buffer and Millipore water, and blown dry with pure nitrogen. To stretch out the DNA, the masks in the Kapton tape were cut as a slit and the sample and liquids for rinsing were applied on one side of the slit and picked up on the other side using a tissue. This resulted in partly stretched DNA molecules on the mica surface.

2.8 DNA origami

DNA origami samples were provided by the Hao Yan Lab at BioDesign Institute, ASU. Triangular DNA origami was chosen as a sample and modified with two Atto655 molecules at known locations.

[5] Van der Waals or hydrogen bonding, which is responsible for the cohesion of the sheets of mica in the crystal.

Triangular shaped origami template was formed according to Rothemund's paper [90]. A molar ratio of 1:5 between the long viral ssDNA M13 (New England Biolabs, Inc.) and the short helper strands, including the unmodified helpers (Integrated Technologies, Inc.) and ATTO655 modified helper strands (IBA GmbH) was used. DNA origami was assembled in 1× TAE-Mg^{2+} buffer (Tris, 40 mM; Acetic acid, 20 mM; EDTA, 2 mM; and Magnesium acetate, 12.5 mM; pH 8.0) by cooling slowly from 90 °C to room temperature. DNA origami was then filtered with 100 kDa MWCO (Amicon) centrifuge filters to remove extra DNA helper strands. The procedure resulted in solutions containing about 1 nM DNA origami.

The samples for combined imaging were prepared by diluting the stock solution 1:10 in 1× TAE-Mg^{2+} buffer and applying a few µl of this solution onto mica on glass (section2.6). After 5 min of incubation, the samples were rinsed with 200 µl buffer and 200 µl of ethanol, successively and blown dry with pure nitrogen.

The illuminating laser light was changed from linear to circular using a quarter wave plate (at 632 nm). Since the orientation of the fluorophores on the DNA origami is flexible, this ensures even excitation of both fluorophores.

2.9 Defocused Imaging

Defocused wide-field imaging of single molecules is an established technique to probe the orientation of a dipole emitter in 3D [91]. Recently, it has been adapted to confocal microscopy [92]. In confocal microscopy, the laser beam is focused to a small spot on the sample surface. The polarisation in this spot is not uniform, which can be used to find the orientation of the molecular dipole. The excitation of the molecule depends on the angle between the dipole moment and the polarisation of the laser and is greatest when the incident light is polarised parallel to its transition dipole. The emission should not depend on the excitation. This means that the fluorescence can be used to measure the distribution of polarisation in the laser spot by scanning the molecule through the focus, which we do in a confocal scan. When the laser is slightly defocused, we get unique patterns in the fluorescence image that allow us to infer the orientation of the molecule by comparing the image to calculated patterns [91]. The Matlab code for this simulation was developed by Joerg Enderlein[6].

Patterns for different orientations of the molecule are calculated using Matlab (2011b 64bit), and compared to the experiment. As a first step, patterns are calculated for a wide range of angles and values of defocusing to be compared visually to the experimental pattern (Figure 18). From this starting point, a search algorithm is performed for angles +/- 10 degrees in steps of 1 degree, and defocusing 100 nm, 200 nm, and 300 nm. For the algorithm, invalid pixels are

[6] Joerg Enderlein, currently at Georg August University Goettingen, Germany

removed from the experimental data (i.e. emission from other molecules or blinking events). To find the best fit, the calculated pattern is subtracted from the data and the standard deviation over the whole image is calculated. For the best fit of all angles and values of defocusing (within the pre-selected range), the offset between calculated pattern and experimental data is adjusted with the same fitting procedure. The search for best angle and focus, and adjusting the offset is run again until the result does not change any more. For the samples prepared for the single molecule quenching experiments, we found that intensity patterns are consistent with orientations of the molecules parallel to the sample surface. In case the experimental data is rather noisy, the patterns can be compared to the data visually.

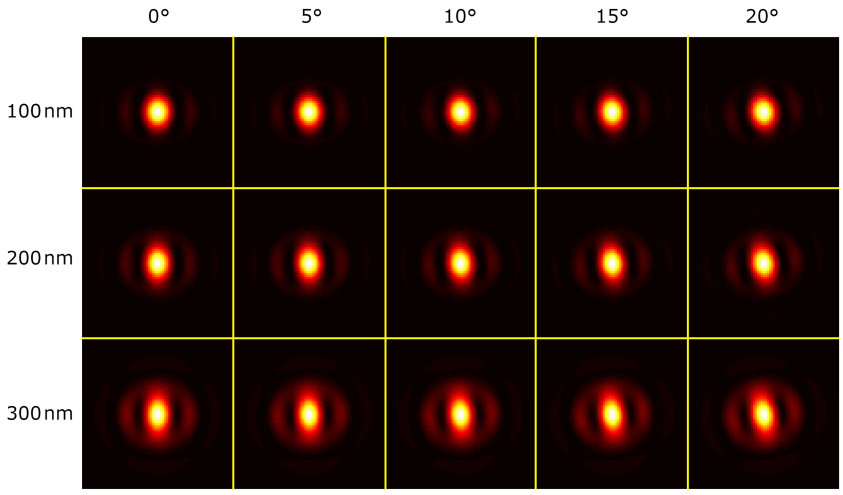

Figure 18

Example of calculated confocal patterns for different positions of the focal plane and for different orientations of the transition moment of the fluorophore. The polarization of the exciting laser light is vertical in the image.

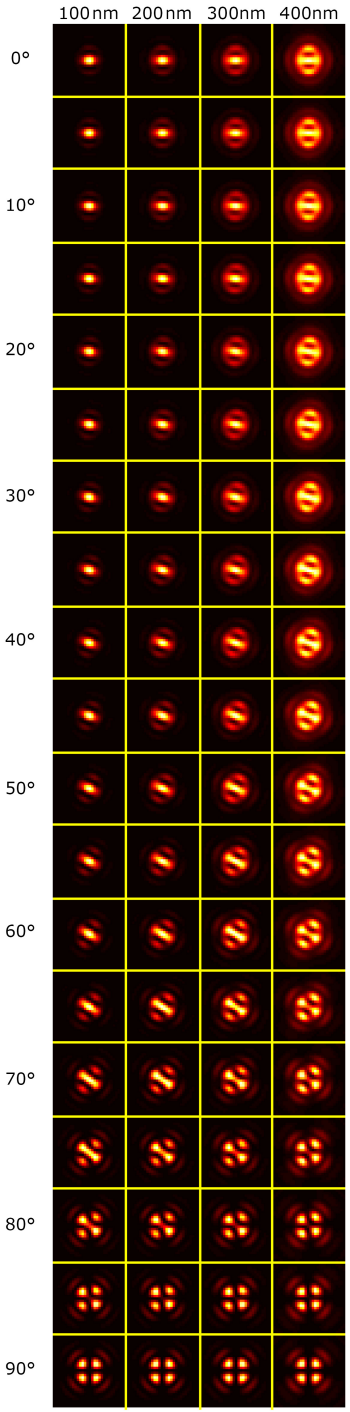

Figure 19

Example of calculated confocal patterns for different positions of the focal plane and for different orientations of the transition moment of the fluorophore. The polarization of the exciting laser light is horizontal in the image.

2.10 Tip model

We are using a classical electrodynamical model and geometrical considerations to calculate the fluorescence of an organic dye on a glass surface in close proximity to a sharp silicon AFM tip. The model is based on the electrodynamics in a system of layered materials, in this case glass, which is the substrate for the molecule, air, which is the imaging medium and the tip material. The Matlab code for this simulation was developed by Joerg Enderlein.

We have modified this model to include the geometry of the AFM tip. We model the AFM tip as a sphere, which corresponds roughly to the very end of an AFM tip (for details of the model, see section 3.2 and Figure 24). The calculations were performed using the following parameters. N(glass) = 1.51, n(air) = 1, n(silicon nitride) = 2, n(quartz) = 1.54, n(Si)@640 nm = 3.84+0.15i, n(Si)@470 nm = 4.49+0.064i [93], NA=1.45. The refractive index of silicon nitride varies with composition. In crystalline silicon nitride the stochiometry is Si_3N_4. In the fabrication of AFM probes this ratio is not fixed, and especially on the surface of the probe, the composition, and thus the refractive index is not known. We chose n=2, which corresponds to crystalline stoichiometry [94].

Since the geometry of the model is symmetric, only one quadrant of the sphere was used for the calculations. This quadrant was segmented into 129 equidistant values for θ and 17 equidistant values for the angle Φ in the x-y-plane. For each value of θ the distance of the point dipole from the point of contact

between tip and surface (x-position) and the shortest distance between fluorophore and tip (*d*) were calculated. The calculation was limited to values of the x-position smaller than 128 nm. With the values for θ and distance, the fluorescence intensity was calculated as follows. The excitation is calculated by the same procedure as used for the calculation of the defocused patterns and is averaged over the entire focal spot. The emission of the excited molecule that is collected by the microscope objective is summed up. These two values are multiplied to give the observed fluorescence intensity. The results are plotted versus x-position and Φ to give a 2D intensity distribution that corresponds to a confocal scan (Figure 24).

2.11 Software

For data acquisition and image processing for the AFM, the Asylum Reasearch Software Version 101010+1006 (Asylum Research, California), based on Igor 6.2.2.2 (Wavemetrics, Oregon) was used.

For the MicroTime200, SymphoTime 5.13 (PicoQuant GmbH, Germany) was used for data acquisition and image processing.

For further image processing Gwyddion 2.26 (www.gwyddion.net) and SPIP 4.5.4 (Image Metrology, Denmark) were used.

For the tip model and the calculations of the confocal patterns, Matlab R2011b was used.

CHAPTER

3 RESULTS

3.1 Combined topographic and fluorescence imaging

To show the capability of the combined setup to collect topographic and fluorescence data simultaneously, we chose stained double stranded DNA as a sample. With a diameter of about two nanometers, DNA is an excellent sample to test the resolution and quality of AFM images. The sample preparation is described in sections 2.6 and 2.7.

The alignment for these experiments was different from the methods described above. The topography and the fluorescence signal from the DNA itself were used to align the AFM tip with the confocal volume[7].

In the images, the topography of the DNA on mica can be clearly distinguished from the background. In the top image, both stretched out and coiled DNA is present. In the fluorescence lifetime image, the stretched out parts of the DNA are well resolved, while the coiled DNA appears as one spot. Some background from unbound YOYO-1 shows as spots in the image where no DNA is seen in the topography image.

The bottom image shows another example of a combined measurement. On the left side, the fluorescence lifetime and the topography image are overlaid to show the alignment between the two microscopes. The slight misalignment of

[7] The easier and more reliable methods using back reflected light as described in section 2.1 (Figure 17) was developed after these measurements were performed.

about 100 nm is due to thermal drift after aligning. The data shows clearly the ability to resolve double stranded DNA topographically while acquiring single molecule optical data.

Another interesting feature of these measurements is the distribution of the fluorescence lifetime of the individual YOYO molecules. The lifetimes are shifted towards lower values, which is consistent with quenching due to the mica described in the literature [95, 96]. Also the distribution of the fluorescence lifetime is wider. This suggests that the mica surface has a non-uniform influence on the fluorophores. It is conceivable that the closeness of the fluorophore to ions inside the mica[8] causes the quenching effect.

[8] Potassium and aluminum for muscovite mica, which was used here.

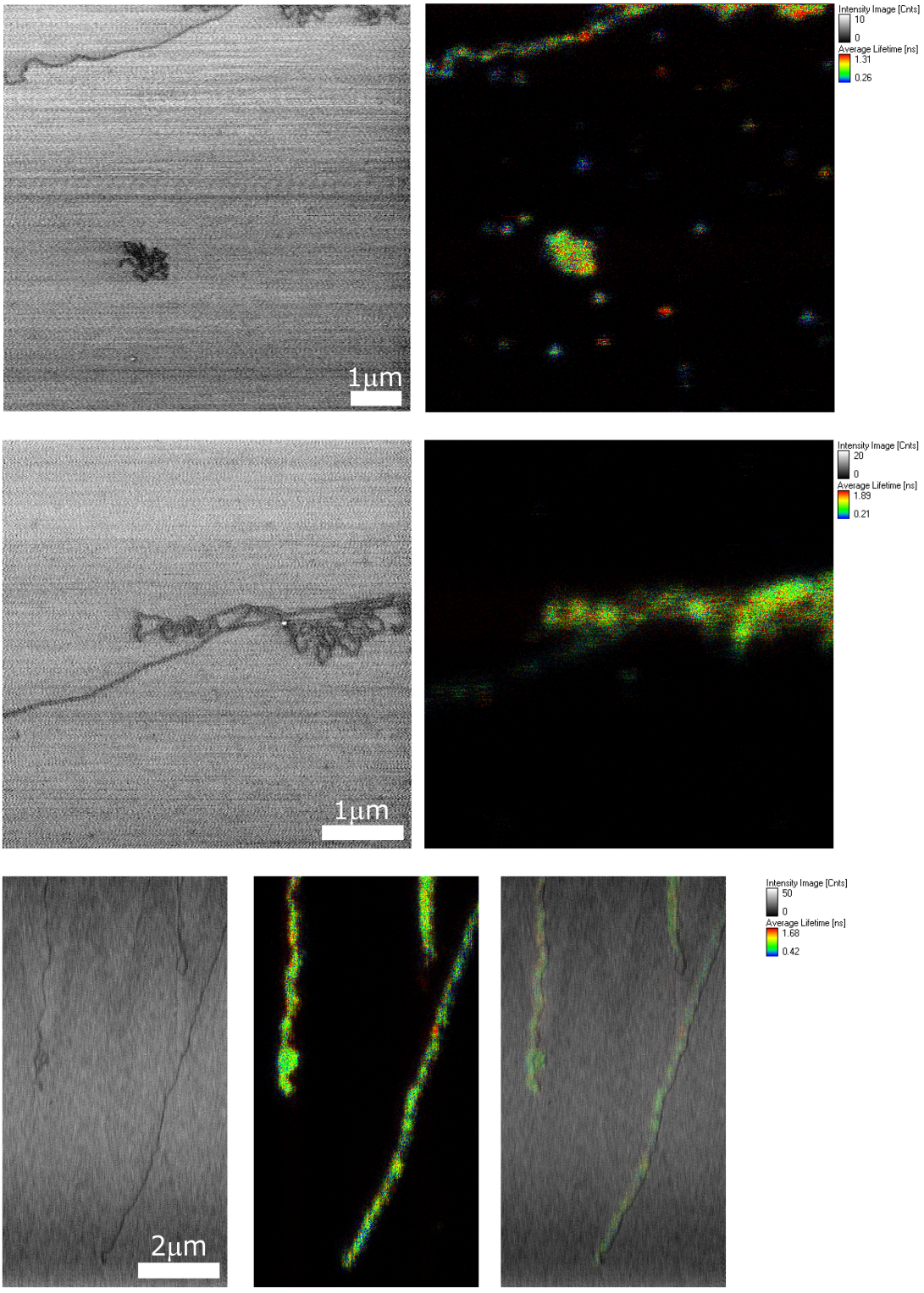

Figure 20

Examples of combined AFM/fluorescence lifetime images of YOYO-1 stained lambda-DNA

3.2 Simulations of tip induced fluorescence modification

A classical electrodynamic model, which calculates the interaction of light with a system of layered materials, was modified to simulate the influence of the AFM probe. The probe was modeled as a sphere, which corresponds roughly to the end of an AFM tip.

The model was used to compare the experimental data with theoretical predictions for the change in fluorescence intensity near the probe. Fluorescence intensity maps for different tip geometries, e.g. spheres and cylinders with curved edges, different wavelengths, different tip materials, as well as different media (air and water), were calculated.

Figure 21 shows the distance dependence of the observed fluorescence intensity of a dipole emitter in front of a silicon half-space, which is above a glass interface (sample surface). As we expect from theoretical predictions and experiments [50], we find oscillations of the fluorescence as the interface is moved away from the molecule. For long distances, the intensity reaches the value without silicon present. Note that this value is not the same for all plots since the spatial distribution of the radiation is different for the different configurations, and the microscope objective collects only part of the angular distribution. Also, the presence of the glass interface changes the emission for a parallel and perpendicular dipoles differently. For very short separations, the intensities for a parallel and a perpendicularly oriented dipole behave differently. For the parallel dipole, we find a strong reduction of the fluorescence, whereas in

the case of a perpendicular dipole the fluorescence is enhanced. In water we find a similar behavior for the parallel dipole with a higher enhancement in the first maximum. In the case of the perpendicularly oriented dipole, we find a strong minimum in the intensity around 150 nm distance and no enhancement for zero distance.

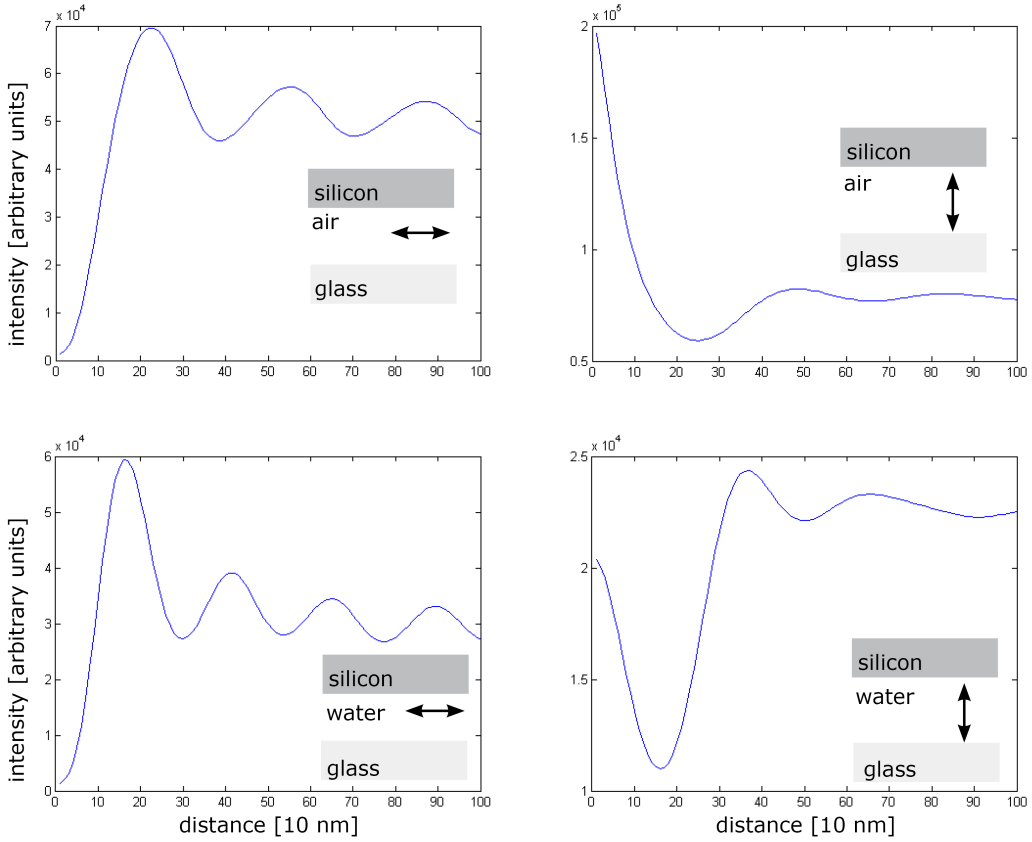

Figure 21

Distance dependence of the fluorescence intensity of a dipole emitter in front of a silicon surface for parallel and perpendicular dipole orientations in air and in water. The wavelength for the calculation is 640 nm.

When the molecule is near the surface of the AFM probe, the situation is different. Not only the distance to the AFM probe changes, but also the angle of the molecule's transition moment to the probe surface changes as the molecule is

moved away from the probe (Figure 23). This leads to a much more rapid change in the fluorescence intensity for movement in direction of the transition moment away from the tip. Danos et al. Have found no significant difference in the influence of different crystal directions of silicon onto the fluorescence of DiO molecules [46], which justifies that we do not take into account the change in crystal direction around the tip. Using defocused imaging (section 2.9), we found that the fluorophores which were immobilized on glass always showed an emission pattern that was consistent with the transition moment oriented parallel to the sample surface. When the molecule is scanned under the AFM probe, the direction to the surface changes from parallel (quenching) to perpendicular (enhancement for short distances). Also the fact that the AFM probe is not an infinite half-space of silicon leads to a quicker change in fluorescence intensity. Both effects are considered in the geometrical model used to calculate the fluorescence near the AFM probe as follows. For every position of the molecule, the fluorescence is calculated without the tip material. This value is subtracted from the fluorescence with the silicon half space present. Figure 22 illustrates this procedure. The resulting value contains the corrected influence from the AFM tip onto the fluorescence and is negative in the case of quenching and positive in the case of fluorescence enhancement. To take into account the fact that the AFM tip is not infinitely extended, we scale this value according to

$$(Fluorescence - Fluorescence_{notip})\left(\frac{r}{r+d}\right)^3$$

where d^{-3} stems from the magnitude of an induced dipole in a sphere as opposed to an infinite plane. Finally, the fluorescence of a molecule parallel to the glass surface without silicon is added to yield the total fluorescence.

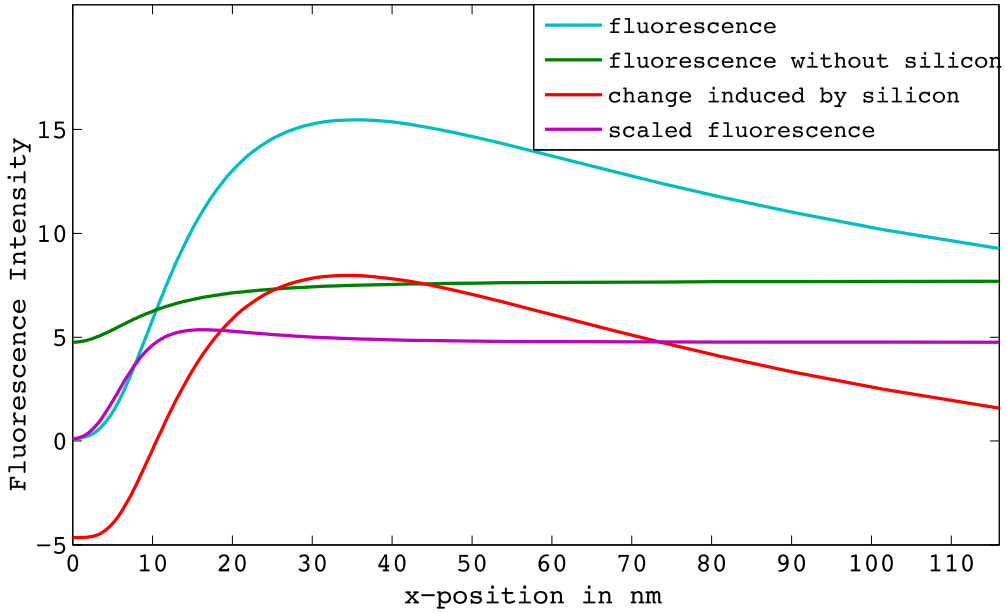

Figure 22

Illustration of the renormalizing procedure. See text for details.

Another approximation of the model is that the tip is centered in the diffraction limited fluorescence spot, and that excitation power and polarization as well as detection efficiency do not change when moving the molecule away from the center. Thus, the model produces "flat" intensity images where a pattern as shown in section 2.9 would be expected. Although this model is rather simple, it reproduces the general trends in the data taken with silicon AFM probes nicely

and is even able to predict correct length scales for the extent of the quenched area and the position of areas of enhancement. For quartz and silicon nitride probes the experimental data shows much stronger quenching than the model predicts. This shall be discussed in section 3.3.4.

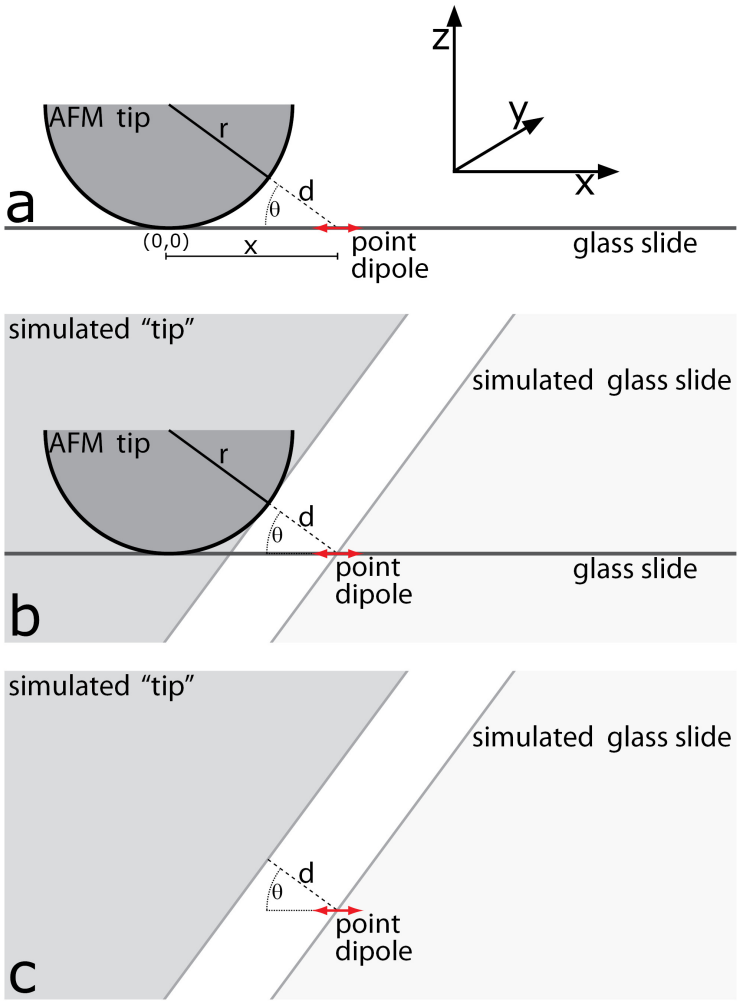

Figure 23

Illustration of the modeling procedure. See text for details.

When we plot the 2D intensity distribution generated by the model (Figure 24), we always see an area of lower fluorescence intensity in the center, when the

molecule is right under the AFM probe. From the center, in the direction perpendicular to the transition moment, we find a steady rise of the fluorescence intensity. In the direction of the transition moment, we find enhancement for silicon probes, but not for silicon nitride and quartz probes. Sections along the direction of the transition dipole moment show how the capability to resolve two emitters, as defined by the FWHM, is expected to improve with sharper probes (Figure 25). For silicon probes with radius 2 nm, 5 nm, 10 nm, and 15 nm, the FWHMs are 2.2 nm, 5.6 nm, 11.2, and 17.2 nm. Silicon probes with 2 nm radius of curvature at the tip end are commercially available. For imaging in contact mode in air, however, the probe will become dull immediately.

The comparison of different wavelengths with this model does not show much deviation (Figure 25). For silicon, the enhancement peak for 470 nm wavelengths is located a little closer to the center than for 640 nm. Results for imaging with blunted tips and imaging in water will be shown in direct comparison with the data in sections 3.3 and 3.4.

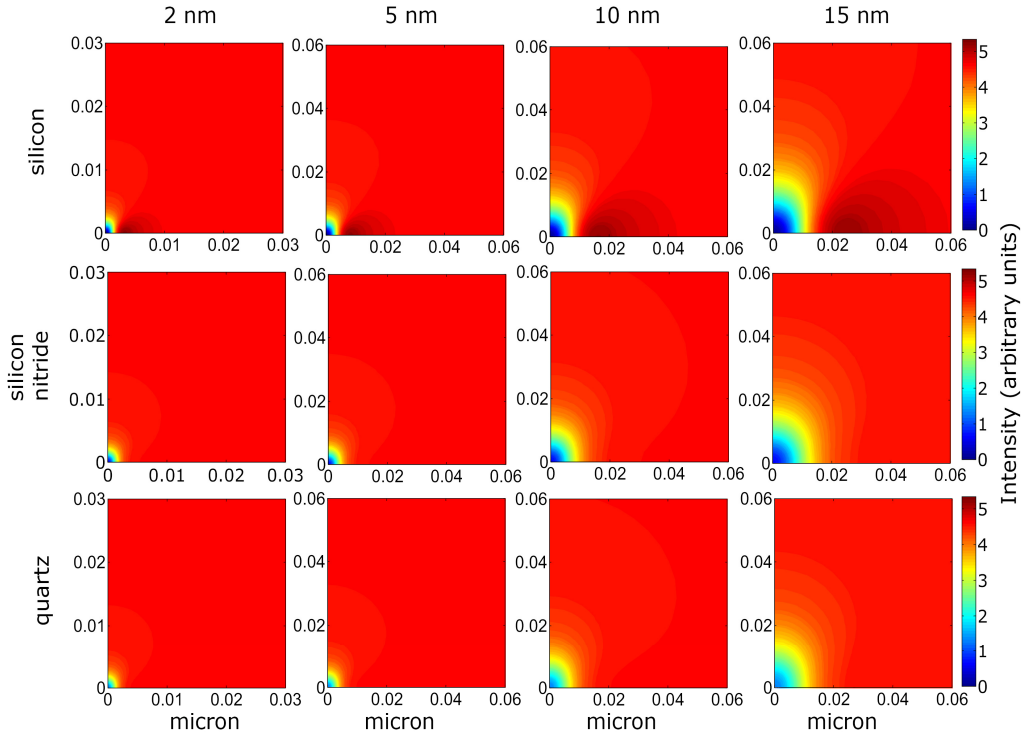

Figure 24

Intensity distribution around the AFM probe generated by the spherical tip model for different tip materials and radii. Since the data is symmetric, only one quadrant is plotted. The wavelength for the calculations is 640 nm, the imaging medium is air. The laser polarization and orientation of the dipole emitter are horizontal in the image. The unit for the positions is micron. Note the different length scale for 2 nm radius.

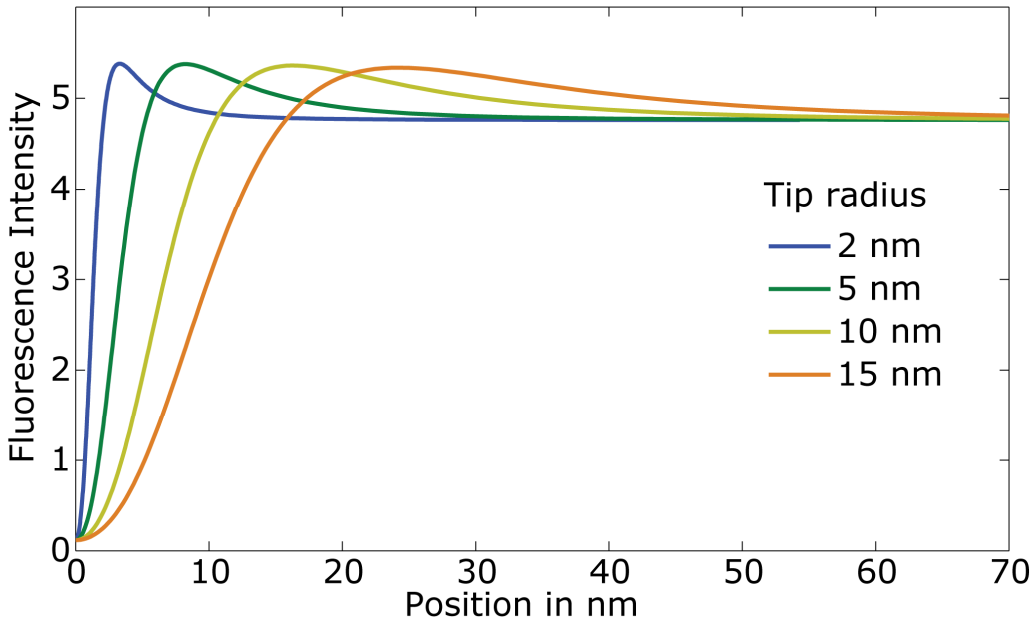

Figure 25

Sections through the center in direction of the transition moment for silicon probes with different diameter. The wavelength is 640 nm

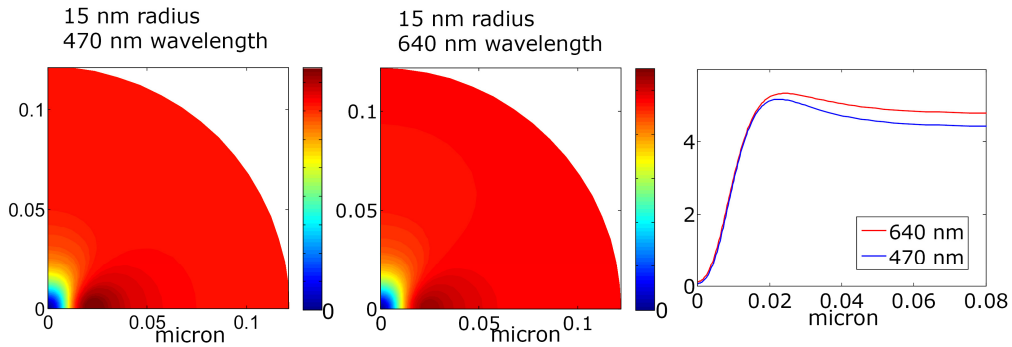

Figure 26

Comparison of different wavelengths for a 15 nm silicon probe. The 2D plots look similar. The section shows that the peak for 470 nm occurs a little earlier and is slightly more pronounced. The intensities were scaled to be comparable.

3.3 Quenching and enhancement of florescence near an AFM probe

When good alignment was provided, every combined AFM/confocal scan showed changes of the fluorescence near the AFM probe. Quenching was always observed, and enhancement in the case of silicon probes. In this section, the extent of the influence of the AFM probe, and experimental results for different tip materials and sizes, and fluorophores will be shown. All the experiments in this section were performed in contact mode AFM under ambient conditions.

The resolution in the image does not only depend on the FWHM given by the interaction between the fluorophore and the AFM probe, but also on the pixel size in the image. To distinctly see a quenched spot, it should be distributed over two or three pixels, which means that the pixel size should be around 2nm for sharp probes. In principle, the number of pixels per image can be chosen arbitrarily large, but then the number of detected photons in a given time has to be distributed over more pixels, and the number of photons per pixel is smaller which leads to a lower signal to noise ratio. Since the total number of photons that a fluorophore can emit before it bleaches is limited, the total intensity cannot be chosen arbitrarily high. Thus, if high resolution data is required, the scan size must be chosen very small. A technical issue with this is drift. It was observed that over time the tip moved with respect to the objective. Realignment of the objective under the tip was required throughout the measurements. However, high resolution data could be obtained and shall be presented in the following sub-sections.

3.3.1 Localization of tip effects

The change of fluorescence was always found to be highly localized near the AFM probe. Few tens of nanometers away from the tip, no change of the normal fluorescence is observed.

Since the fluorescence of one molecule is not spatially uniform, but rather creates the patterns shown in section 2.9, the influence from the tip needs to be deduced from the difference of a scan with the AFM probe aligned and in contact and a scan with the AFM probe retracted[9]. Figure 27 shows three different scans of a sample of Atto655 on glass, where two scans of the same area, one with tip approached, one with tip retracted, are compared side by side. The scans show the typical single molecule patterns. Also blinking and bleaching can be seen, which obscures the comparison between the scans somewhat. However, we can see that the general shape of the spots is not altered by the AFM probe, but we a distinct change in the fluorescence intensity, namely darker triangular spots and brighter regions above and below, in the center of the patterns. The time for one scan was 4 min 16 sec. Differences in the brightness and slight changes in the shape of the pattern between the two scans can be explained by slightly fluctuating laser power and thermal drift of the focal plane.

[9] The AFM can perform its normal scanning routine with the AFM probe piezo fully retracted. The AFM tip is then about 10 micron above the surface.

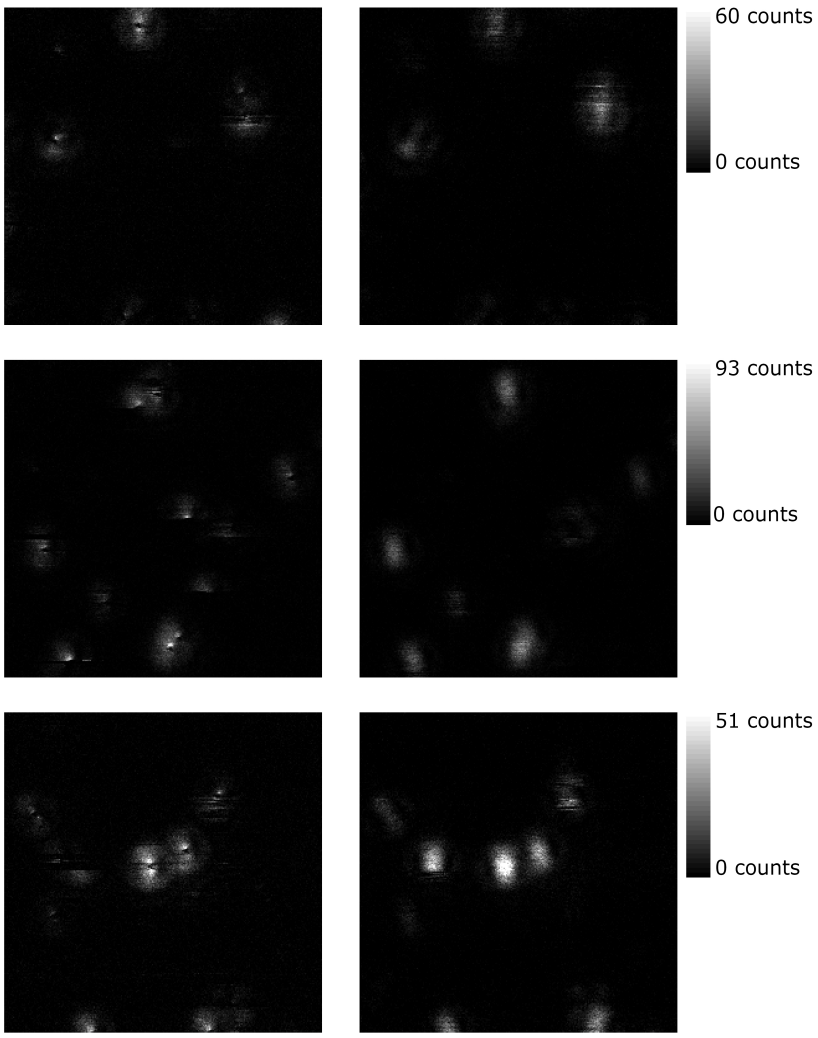

Figure 27

Comparison of combined scans with the AFM tip approached (left) and retracted (right). The images show fluorescence intensity from Atto655 molecules on glass. The laser polarization is vertical in the image.

The high localization of the tip effects leads to the ability to produce very small spot sizes, which ultimately lead to high resolutions in the optical image. As of now, typical spot sizes in near-field microscopy with AFM are 10-20 nm. As mentioned in Chapter 2, Jordan Gerton's group was able to produce much smaller spot sizes using fluorescence enhancement with silicon probes. Their typical spot

size is given with 8 nm. Using quenching, we were able to achieve spot sizes below 5 nm. Since the AFM was operated in contact mode, and the probes become blunt after some time of scanning or if the first approach of the tip is rougher than desired (see next section) a typical spot size is difficult to determine. With new probes and smooth approach, spot sizes between 5-15 nm were common. Figure 28 shows a few examples of small spots.

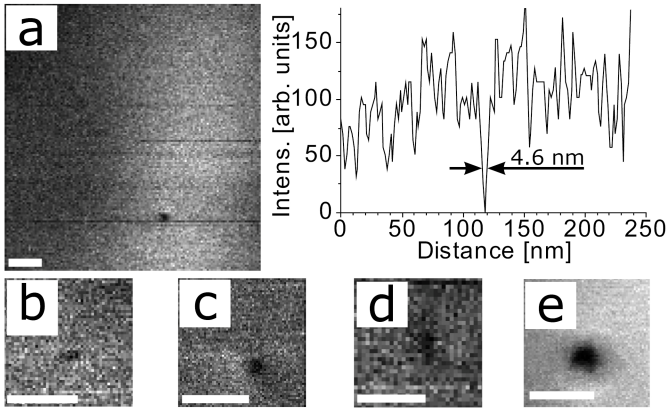

Figure 28

Combined scans of Atto655 with silicon AFM probes. The scale bars are 50 nm in all images. The graph on the right shows a section through the center of the quenched spot in (a).

The smallest spot size achieved so far is 4.6 nm (FWHM). The corresponding scan is shown in Figure 28(a). This was the fifth scan in contact with the same tip. The FWHMs for (b), (c), (d), and (e) are 6.8nm, 7.5nm, 5.9nm, and 16nm. These are scans with different samples and different probes. The high resolution scan in (e) reveals fluorescence enhancement above and below the AFM probe as predicted by the theory. Scans of this quality are highly dependent on the stability of the dyes. In the scans prior to the one shown in (a) for example,

the molecule bleached before effects from the tip could be observed. Also drift of the tip with respect to the laser focus interfered with the measurements. A one step zoom-in to high resolution often resulted in no tip effects to be observed because the tip had moved out of the scan region.

3.3.2 Imaging with blunt probes – fluorescence enhancement

During all measurements, the AFM probes became dull because of interaction with the surface. This prohibits small spot sizes in the optical image and is desired to be avoided for high resolution imaging. An advantage of dull tips is that the effects of the probe onto the molecule can be seen more clearly. The area where the fluorescence is quenched appears in the shape of the end of the AFM probe, which is triangular in the case of standard silicon probes. Fluorescence enhancement along with a shortened fluorescence lifetime is prominent besides the tip (Figure 29). Comparison with calculated patterns of the confocal spots shows that the change in lifetime and fluorescence enhancement occurs along the direction of the transition moment of the fluorophore (compare Figure 24). With the probe used here, the change in lifetime is not symmetric though. We would expect similar behavior on both sides of the AFM tip, but in the scans it appears that there is much stronger fluorescence enhancement along the upper edge of the probe. This can be explained by a sharper edge, or an angle between the tip and the surface, which leads to one edge being in contact while the other edge remains separated from the surface. Imaging the probe with the

electron microscope confirms the triangular shape of the end of the AFM probe.

To model the data with blunted probes, the model described in section 2.10 was modified. Instead of a sphere, the modification assumes a cylinder, which is curved at the edges. The calculations are performed as described in section 2.10, with the radius of the sphere now being the radius of curvature of the edge of the cylinder. For the scaling procedure, the radius is exchanged by the radius of the cylinder. Clearly, this model does not capture the truncated pyramid shape of the AFM probe, but it is able to reproduce the strong fluorescence enhancement which we see in the data.

An example is shown in Figure 30. The model data was calculated with a radius of the cylinder of 52 nm, the radius of curvature on the edges is 2 nm. The wavelength is 640 nm, the material is silicon. Because of symmetry, only one quadrant of the data is shown. The result shows strong enhancement (about 2 times) above the AFM probe in direction of the laser polarization and the orientation of the dipole's transition moment. For comparison, high resolution data taken with blunted probes is shown. The middle panel shows data acquired in a combined measurement with a standard silicon AFM probe. We can see strong enhancement in the direction of the transition dipole, which can be inferred from the elongation of the confocal pattern. Very interesting to note is the crescent shape of the enhanced region, which is not captured by the model. It is possible that interactions with higher parts of the tip, where the distance of the molecule to the tip falls into the second maximum (compare Figure 21) cause this effect.

Another explanation is that the scaling, which we know is a coarse approximation, does simply not capture this effect. It could be that the outer regions of the crescent shape are due to interaction with the tip in the first maximum after quenching. The distribution of fluorescence lifetimes (bottom image) is consistent with a radiative enhancement mechanism as predicted by the model. The right panel shows data taken with a conical AFM probe[10]. The probes are fabricated by etching in an ion beam and do not exhibit the pyramidal shape which results from anisotropic wet etching of silicon in the standard fabrication process. The data shows quenching in the middle and enhancement above and below the tip. Again, we can see the crescent shape of the enhanced region.

[10] CFM conical probe, AppNano

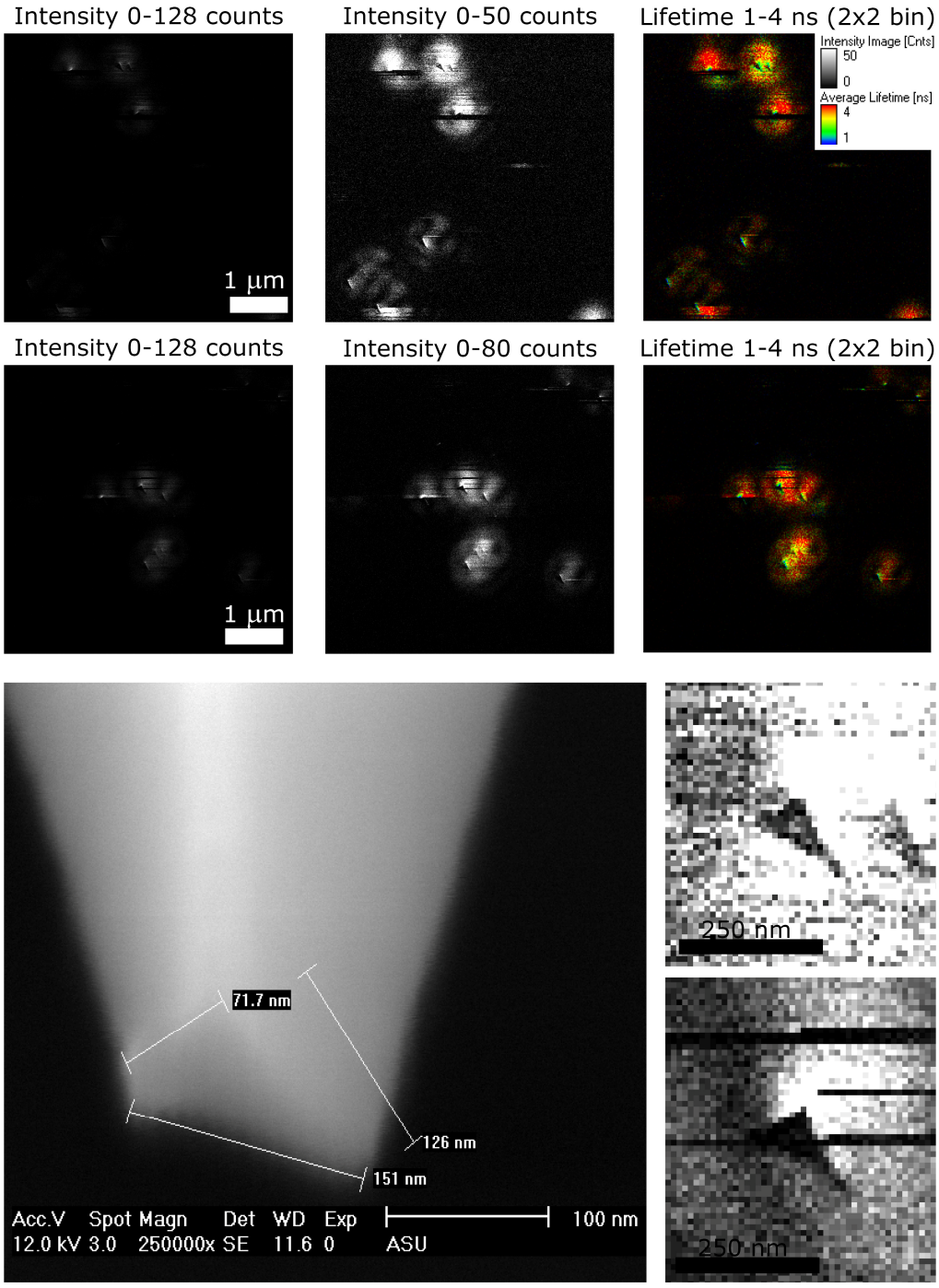

Figure 29

Combined images with a blunt silicon AFM probe. The first and second row show intensity images at two different color scales and fluorescence lifetime from two different scans with the same tip. The bottom left shows a scanning electron image from the AFM probe used. On the bottom right are two enlarged views from the combined scans.

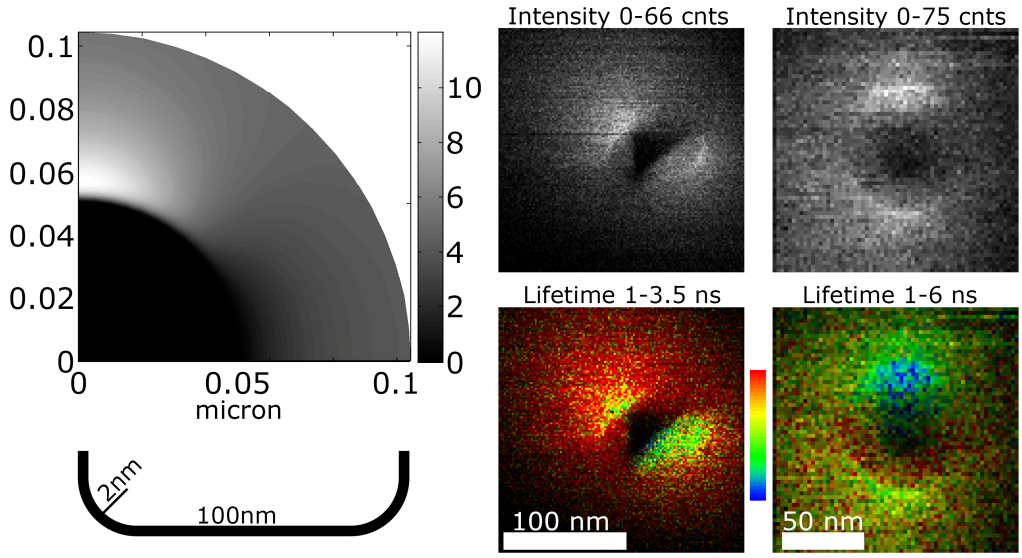

Figure 30

High resolution combined images with a blunt silicon AFM probe and comparison with the model. On the left is the calculated intensity image. The middle shows fluorescence intensity (top) and fluorescence lifetime (bottom) of a combined scan taken with a regular blunted probe. On the right is intensity (top) and lifetime (bottom) of a combined scan taken with a blunted conical probe.

3.3.3 Comparison of different fluorophores and emission wavelengths

The question arises, whether the modulation of fluorescence due to the AFM probe stems only from unspecific interactions or if it has to do with the particular chemistry of a fluorophore or a certain energetic transition in the AFM probe. The role which the AFM probe plays will be addressed by comparing different tip materials (section 3.3.4). Whether the chemistry of the fluorophore or a particular interplay of AFM probe and fluorophore plays a dominant role, was checked by using different fluorophores with different chemical structures and different ranges of emission wavelength. Three classes of fluorophores were

compared, namely derivatives of oxazine (Atto655), rhodamine (Alexa488), carbo-rhodamine (Atto647N) and cyanine (Alexa647). The choice of wavelengths was limited by the experimental setup, since only excitation with 470 nm and 640 nm was possible, which are, however, the upper and lower end of commonly used excitation wavelengths. A technical problem with excitation at 470 nm was higher auto-fluorescence from the sample surface and stronger blinking and faster bleaching of the fluorophores.

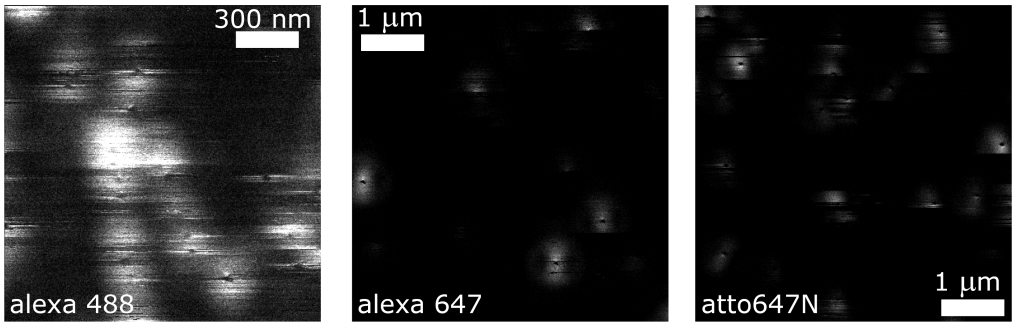

Figure 31

Qualitative comparison of three different fluorophores imaged with a silicon AFM probe.

Figure 31 shows the data from combined scans with Alexa 488, Alexa 647 and Atto 647N. All three scans were taken with a slightly blunted AFM probe. Thus, a triangular dark spot in the confocal pattern can be observed. Above and below the quenched spots, an area of higher fluorescence intensity can be seen. The fact that all three fluorophores behave similarly in the combined measurements leads to the conclusion that the particular chemistry of a molecule is not a crucial factor for the quenching mechanism.

3.3.4 Comparison of different AFM probe materials

The experimental data presented so far has been acquired in combined measurements with silicon probes. Most near-field optics using pointed probes makes use of metal or silicon tips to enhance the optical signal in a region much smaller than the diffraction limit, as discussed in section 1.4. One publication presents experimental data from combined AFM/fluorescence measurements using a silicon nitride probe [97]. They embedded fluorophores in a polymer matrix for their experiments, and they found a reduction in fluorescence intensity and a shortened fluorescence lifetime when the fluorophore is under the tip. However, the spot size for the reduction in fluorescence intensity is rather large (about 100 nm), and the efficiency of quenching is given with 50%[11]. The data is explained using a classical model similar to the one used in this work, however, the change in orientation of the transition moment to the surface of the tip is ignored. In our experiments, we found very efficient and highly localized quenching with both silicon nitride and quartz AFM probes, which contradicts the classical model. Figure 32, Figure 33, and Figure 34 show high resolution data for silicon, silicon nitride, and quartz probes. In the intensity images, a very distinct quenched spot can be seen. The fluorescence lifetime images reveal a shortened lifetime near the tip in the direction of the transition dipole of the fluorophore and a longer lifetime in the perpendicular direction. This is consistent with radiative enhancement and inhibition of fluorescence. Very close to the tip a lower

[11] The data presented in the paper is not clear in this respect, since the background level of fluorescence intensity is not given.

fluorescence lifetime can be observed in the region with less fluorescence intensity. This would indicate non-radiative energy transfer near the probe [98]. However, the correct analysis of fluorescence lifetime statistics to determine the nature of a process that modifies fluorescence emission requires detection of all photons from a sample, or rather a representative distribution of photons from all directions. In the case of our combined AFM/fluorescence measurements however, we are restricted to collecting photons from a finite angle, given by the numerical aperture of the objective. The presence of the AFM probe changes the spatial distribution of the emission from the fluorophore. Thus, a rigorous analysis of the lifetime data is not possible and one must be careful with interpretation of the data.

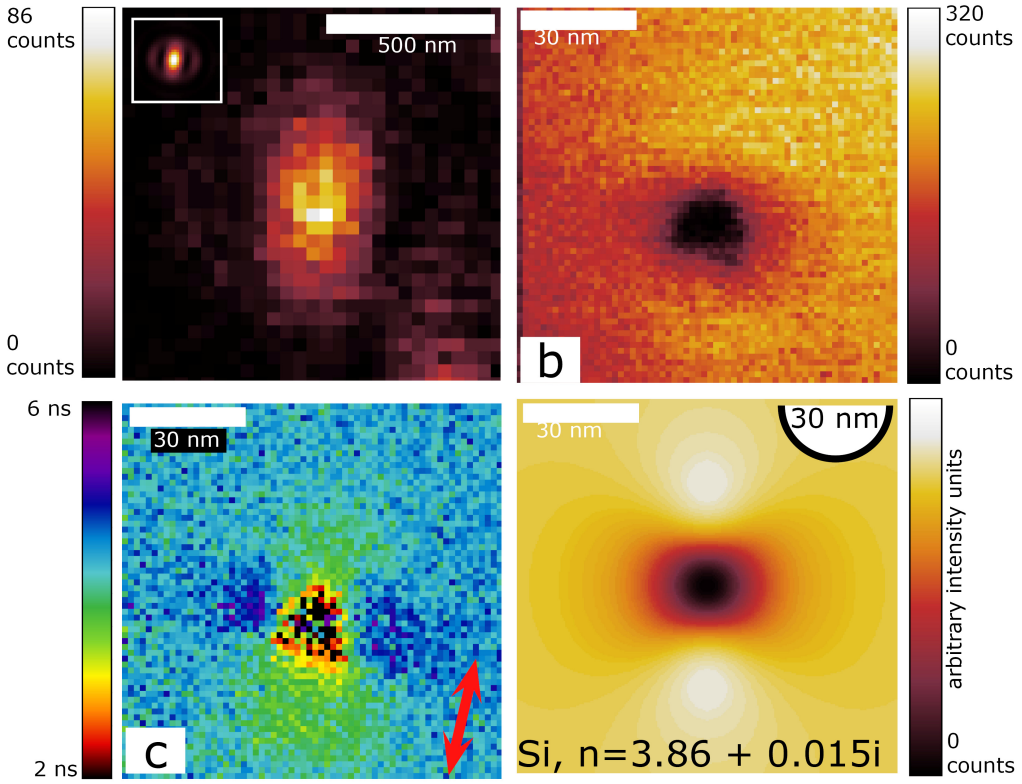

Figure 32

High resolution data of Atto655 images with a silicon AFM probe. Top left: Defocused image to determine the orientation of the molecule's transition moment (red arrow in the bottom image). Top right: Fluorescence intensity. Bottom left: Fluorescence lifetime. Bottom right: modeled data for a 30 nm radius sphere.

For all three tip materials that we investigated, we find very efficient quenching of fluorescence directly under the tip. Figure 35 illustrates the procedure for determining quenching efficiencies. From a confocal scan where the quenched spot is clearly visible, the background ($I_{backg.}$) is determined from a bleaching or blinking event in close proximity to the quenched spot (blue arrow in Figure 35). Although this method allows only certain scans to be used for evaluation, we believe it to be most accurate, since possible emission from nearby molecules would be taken into account. The intensity in the quenched region

($I_{quench.}$), is taken from the middle of the spot from an area of at least 4 pixels (red arrow in Figure 35). The normal intensity from a region where there seems to be no influence from the AFM probe is taken for reference ($I_{norm.}$, yellow arrow in Figure 35). The relative intensity in the quenched spot is then calculated according to

$$I_{rel.quench.} = \frac{I_{quench.} - I_{backg.}}{I_{norm.} - I_{backg.}} \quad \textbf{(2)}$$

.

The efficiency of the quenching process is 1- $I_{rel.quench.}$. For all three tip materials, we observed very efficient quenching, higher than 96% for all three kinds of AFM probes. In the case of silicon nitride and quartz, this is in contrast to electrodynamic theory and experimental results by Trabesinger et.al. [97]. An explanation of this unexpected strong quenching involves the pressure which the AFM probe exerts onto the molecule. As discussed in section 1.2.4, page 18, pressure onto fluorophores in a host matrix leads to a red shift of the fluorescence. It is possible that we are observing a similar effect here. If the fluorescence of the molecule under the AFM probe is red-shifted, the emission might be outside the detection window in our setup of about 650-690 nm for red emitting fluorophores. The adhesive forces between surface and AFM tip are enough to create pressures of a few GPa, which could induce a large enough red shift of the emission.

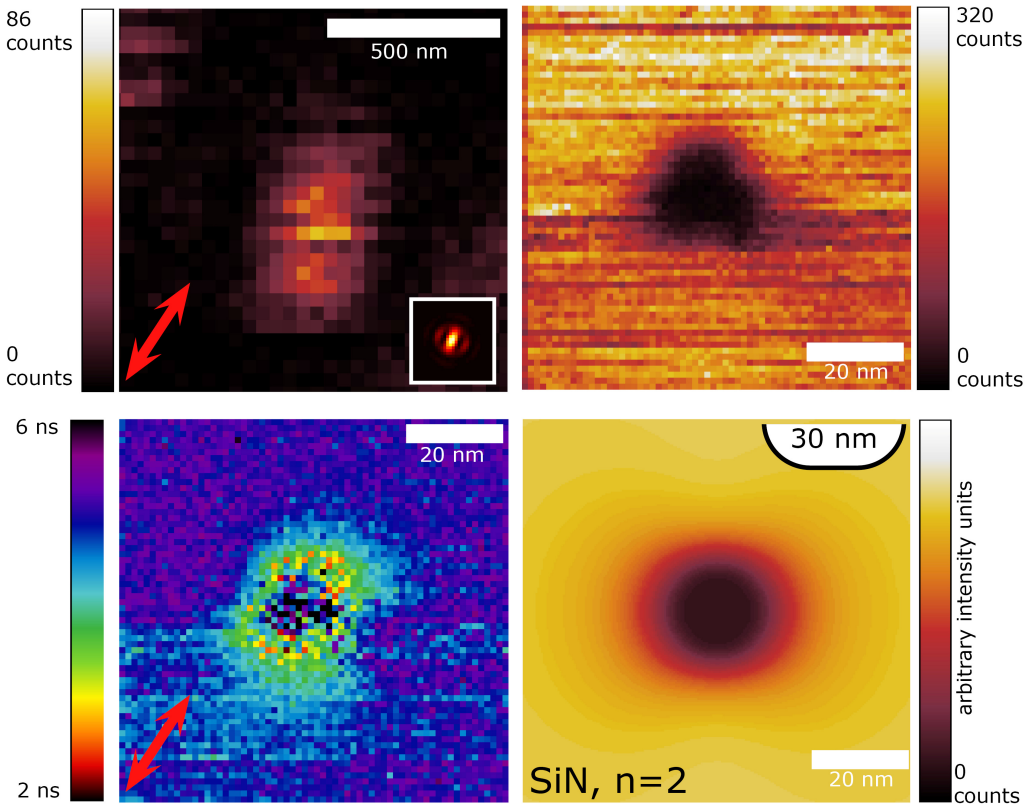

Figure 33

High resolution data of Atto655 images with a silicon nitride AFM probe. Top left: Defocused image to determine the orientation of the molecule's transition moment (red arrow in the bottom image). Top right: Fluorescence intensity. Bottom left: Fluorescence lifetime. Bottom right: modeled data for a 30 nm radius cylinder with 10 nm radius of curvature on the edges.

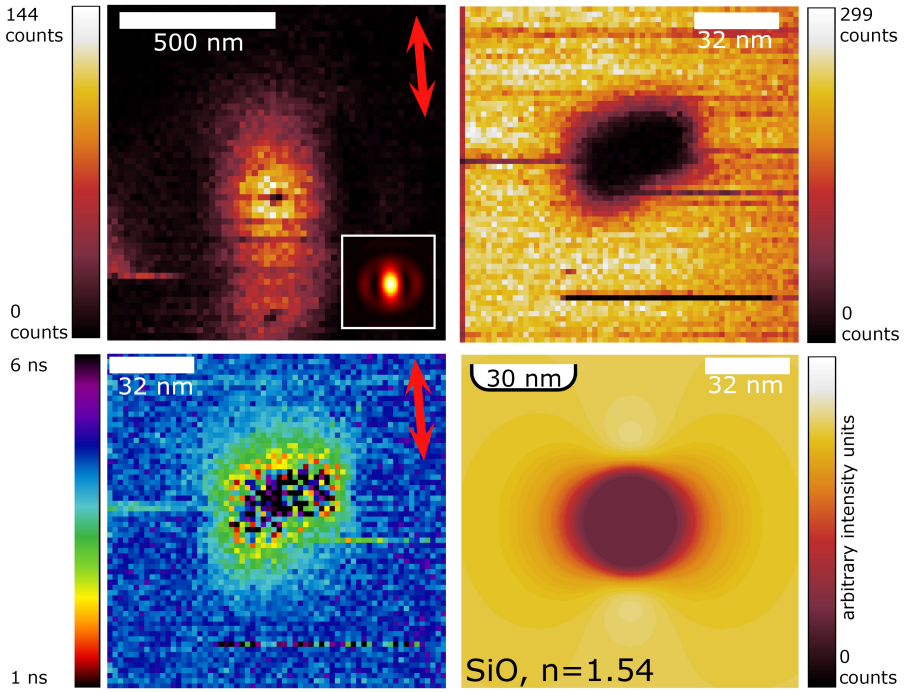

Figure 34

High resolution data of Atto655 images with a quartz AFM probe. Top left: Defocused image to determine the orientation of the molecule's transition moment (red arrow in the bottom image). A second molecule can be seen at the bottom of the image. Top right: Fluorescence intensity. Bottom left: Fluorescence lifetime. Bottom right: modeled data for a 40 nm radius cylinder with 5 nm radius of curvature on the edges.

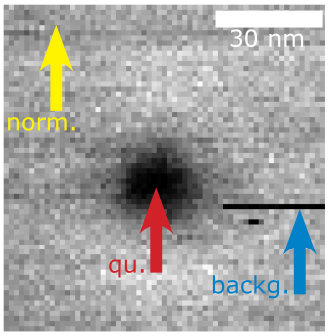

	Si	SiN	SiO
quenching efficiency (exp. data)	97.4% +/- 1.7%	96.3% +/- 2.1%	96.4% +/- 3.3%
quenching efficiency (model)	97.5%	86%	71%

Figure 35

Efficiency of quenching. The background is determined from a bleaching or blinking event during the scan (blue arrow). This background is subtracted from the intensity in the quenched spot (red arrow) and the unmodified intensity (yellow arrow). The relative quenched intensity is calculated according to equation 2. The table shows the values for the quenched intensity for the different tip materials as extracted from the data. The numbers are mean value and standard deviation for several different scans. The sample sizes are n=8 for silicon (Si), n=2 for silicon nitride (SiN), and n=5 for quartz (SiO). For comparison the values from the model calculations are given.

3.3.5 Evaluation of noise

The lifetime data in all images is the average arrival time of the photon after the laser pulse. For a mono-exponential decay this is the same as the fluorescence lifetime which is determined by fitting an exponential to the histogram of arrival times. Good fits are produced for about 10000 photons. In an image with about 3-300 counts per pixel, a fit for every pixel gives very poor results. The average lifetime however gives fairly smooth images. To evaluate the source of noise in the average lifetime data, we ran Monte Carlo simulations. The geometric model (section 2.10) was used to generate intensities for each pixel in a combined scan. In case that only radiative processes play a role, the

fluorescence lifetime is inversely proportional to the intensity (compare section 1.2.4). For each pixel, we get a fluorescence lifetime by generating N random photons following Poisson statistics, which is normalized by the inverse of the count rate N at that pixel. Background is generated by adding three random photons to each pixel, two of which have a short lifetime (scattering), and one photon has a completely random lifetime within the detection window.

Figure 36 shows the results of the simulations in the case of a 15nm radius silicon AFM tip, and experimental data with a silicon probe. Further away from the tip, where radiative processes dominate the influence of the AFM probe, the experimental data and the generated data correspond fairly well. Close to the tip, non-radiative processes play the dominant role and the model fails to reproduce the experimental data. Also, the intensity in the experimental data is at background level in a more extended region than what the model predicts. Figure 36 (e) shows background generated by the procedure described above. Apart from longer lifetime photons, the qualitative appearance of the plot corresponds to the fluorescence lifetimes in the center of the quenched region in the experimental data. Thus, we can say that the noise of the fluorescence lifetimes is consistent with the random nature of photon arrivals. Also, this comparison allows us to confirm that non-radiative processes play a role near the AFM probe, as would be expected from experimental results in the literature [50].

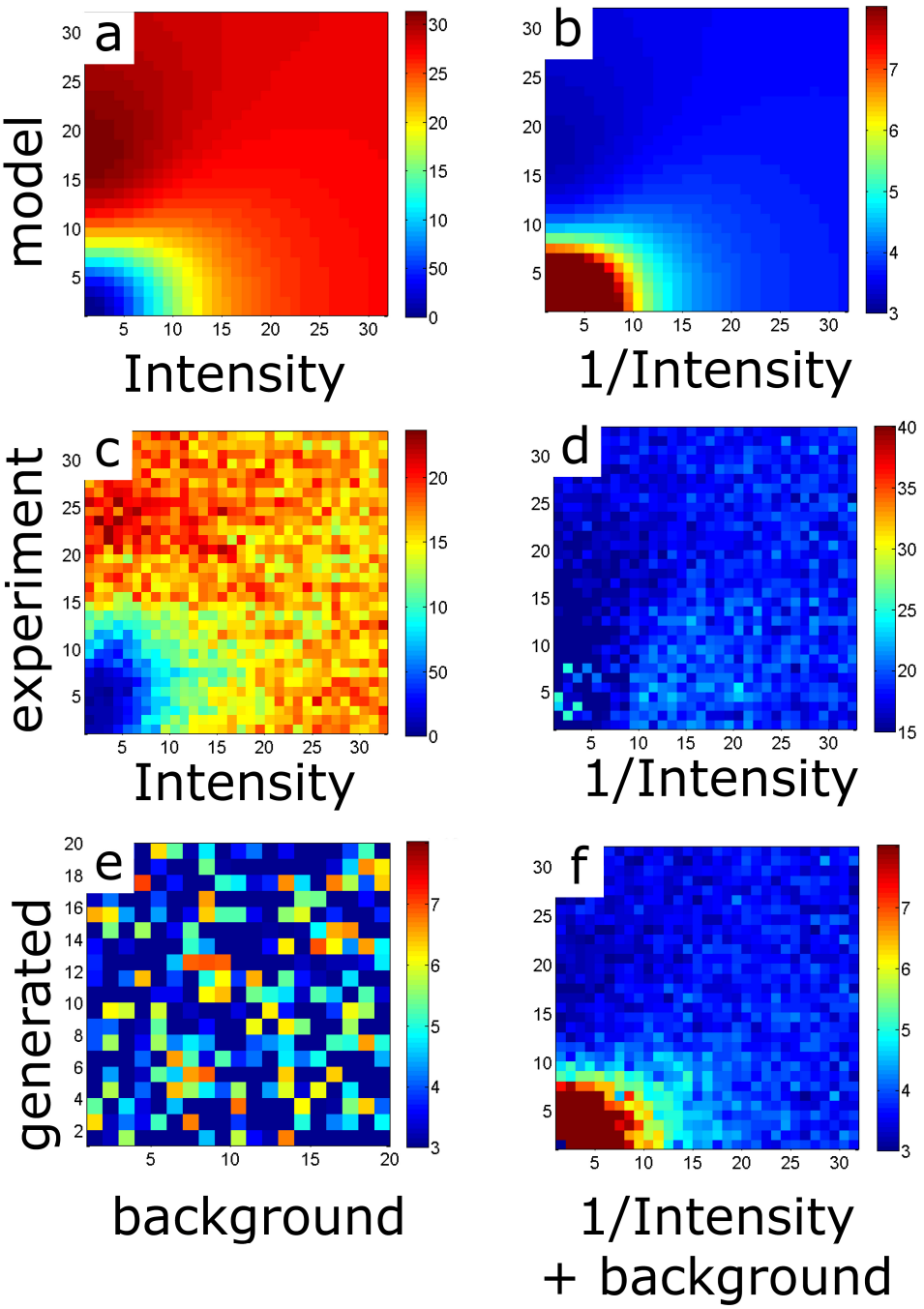

Figure 36

Modeled data, experimental data, and results of a Monte Carlo simulation of the influence of an AFM probe. (a) and (b) show the intensity and the radiative lifetime as calculated by the geometric model (section 2.10). In (c) and (d) the corresponding experimental data is shown. (e) is a plot of random background taking into account scattering of laser light and random photon count events. (f) shows a plot of the lifetime data as generated by a Poisson process.

3.4 Combined AFM/confocal in liquid

In principle, combined imaging in liquid should be advantageous because of less tip-surface interaction, which keeps the tip sharper, and a smaller quenching spot size (see below). However, fluorescence blinking and bleaching interfered with the measurements. Since no closed fluid cell was available for the combined measurements, using chemical modification of the imaging buffer proved very difficult. An oxygen scavenging system[12] along with a ROXS[13] was used to remove free oxygen radicals and depopulate the triplet state of the fluorophore, in this case Atto647N. However, the effect of the buffer wore off very quickly, which made combined measurements all but impossible. It is likely that evaporation of the liquid changed the concentration of the ROXS and exchange with oxygen from the air quickly depleted the oxygen scavenging system.

Another set of experiments was performed using immobilized Atto655, a dye that has proven to be very stable for measurements in air. Unlike Atto647N, the stability of Atto655 is not improved when using ROXS buffers [16], on the contrary, the fluorescence becomes more unstable. For this reason, and for simplicity, we used pure water (Milipore) as the imaging liquid. Under these conditions, the fluorescence was still rather unstable, but some molecules were stable enough to complete a combined measurement. Figure 37 shows the results

[12] Catalase/Glucose oxidase/Glucose

[13] Reducing Oxidizing System, in this case methyl viologen and ascorbic acid (compare section 1.2.4)

of a combined AFM/fluorescence measurement of Atto655 in water with a quartz AFM probe. In the overview scan, three stable molecules and many intermittently fluorescing molecules can be seen. A zoom-in scan at 700 nm size reveals the quenching from the AFM probe a little bit below the center of the molecule. A final zoom-in at 96 nm reveals the shape of the end of the AFM probe. The intensity in the quenched spot goes down to background level, where the model predicts 36.8% of the full intensity in the center.

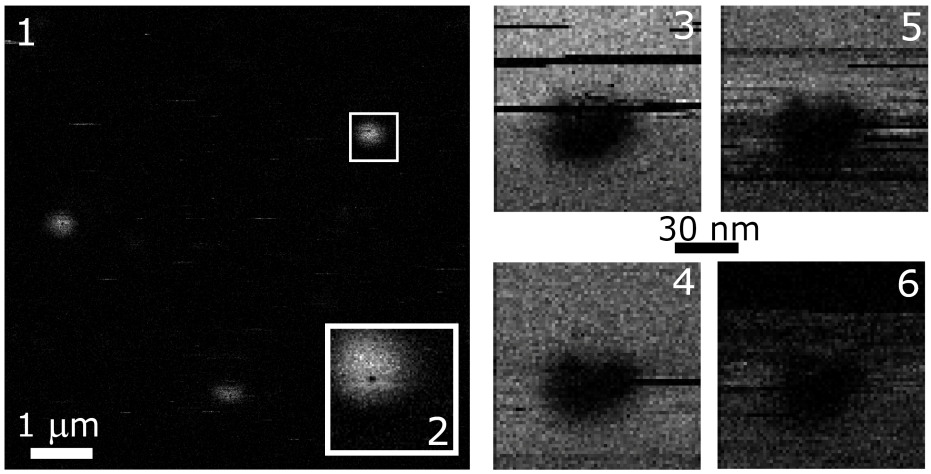

Figure 37

Atto655 imaged with a quartz AFM probe in water. The overview scan (1) shows three stable molecules and stripes in the background which are indicative for intermittent fluorescence of other emitters. The first zoom-in scan (2) reveals the quenched spot from the AFM probe. Scans 3-6 were taken consecutively. The molecule finally bleaches during scan 6. The slow scan direction is down for 1,2,3, and 5 and up for 4 and 6.

The same AFM probe was used to image Atto655 on glass in air, and a high resolution scan was taken right before the measurement in liquid. This allows to directly compare the results from the scan in liquid to a scan in air. Figure 38 shows two combined scans of Atto655 immobilized on glass, measured

with the same quartz AFM probe. It is striking that the image in taken in water looks crisper than the scan in air. The shape of the AFM tip can be made out in the scan in water, whereas it is blurred in the scan in air. We can explain this effect when we consider the electromagnetic effect of the AFM probe onto the fluorescence of the molecule as calculated by the model, and another effect, that is independent of the tip material as discussed in the section before. The model shows that the influence of the quartz probe is higher in air, where it predicts a quenching efficiency of 71%. For quartz in water, the efficiency is only 63.2%. Also, in the case of water, the influence of the tip drops off slower than in air. Thus, the effects that lead to efficient quenching appear more prominent for images in water.

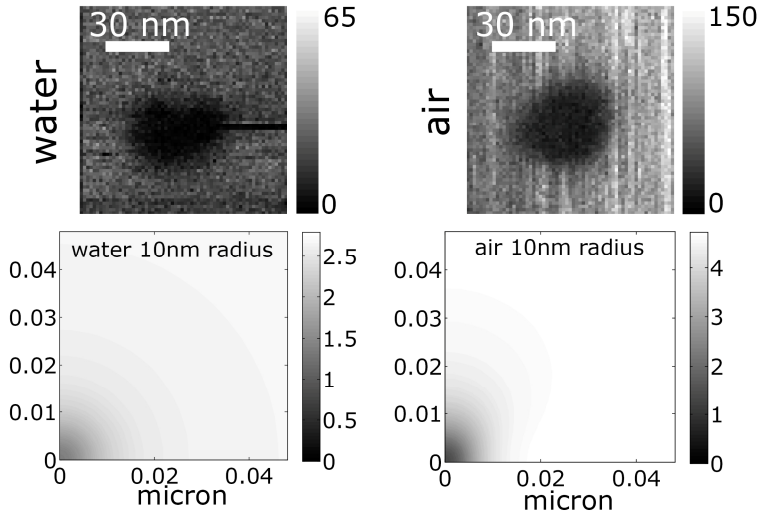

Figure 38

Atto655 imaged with a quartz AFM probe in water and air.

Scanning with a new AFM probe shows the advantage of using imaging in liquid to prevent the tip from becoming dull during the measurement and the

possibility to produce smaller spot sizes. Figure 39 shows two combined scans of the same molecule with a new quartz AFM probe. The FWHM of the spot is 14 nm, which is smaller than any spot measured in air, where the smallest size was 26 nm for a new probe.

With a silicon probe, which should be sharper than a quartz probe, a spot size of 5 nm (FWHM) could be obtained (Figure 40). This is comparable to the smallest spot size that was achieved for imaging in air. The model shows that no enhancement is to be expected for imaging in water. For very sharp tips (2 nm radius), the model predicts a FWHM of the quenched spot of 2.6 nm, which is a little higher than for imaging in air, however, in liquid it is more likely that the probe stays sharp due to reduced interaction with the surface.

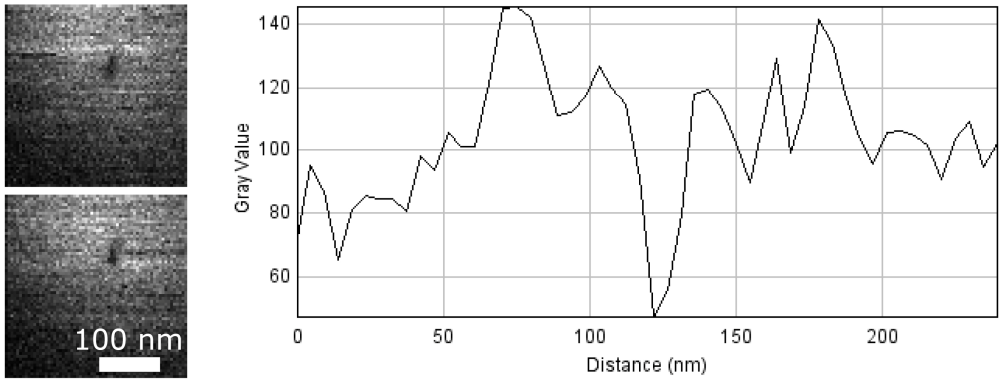

Figure 39

Atto655 imaged with a quartz AFM probe in water. On the left are the lifetime images of two consecutive scans. The right side shows a section though the quenched spot of the top image.

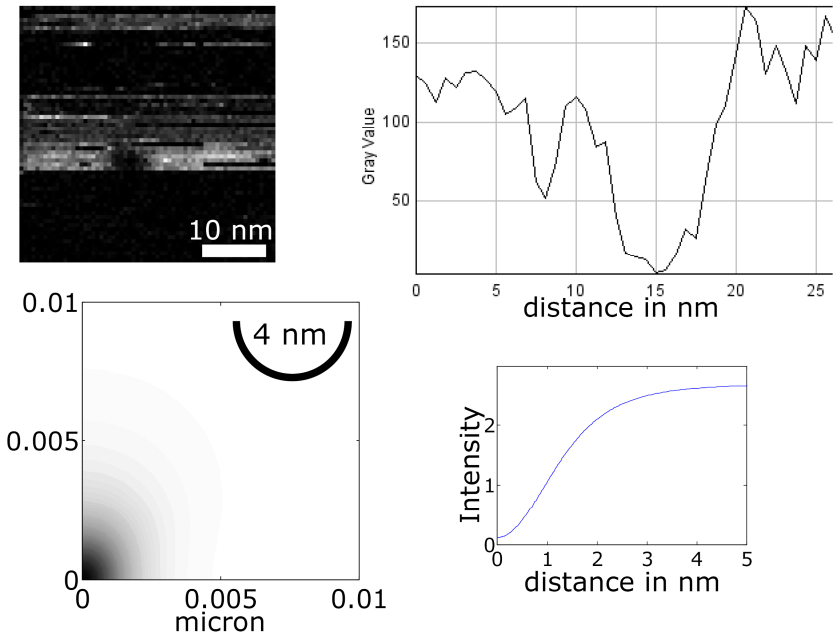

Figure 40

Atto655 imaged with a silicon AFM probe in water. The fluorescence intensity scan and the section (top) show a quenched spot with 5 nm size. The model shows that for imaging in water, no fluorescence enhancement is expected and that the spot size can be as small as 2.6 nm (FWHM) for a 2 nm radius probe.

3.5 Topography and super-resolution fluorescence

A clear advantage of AFM based near-field microscopy is to gather topographic and super-resolution optical information from a sample. So far, only few experiments have successfully shown high resolution data in the topographic and the optical image [67], whereas good AFM resolution with regular diffraction limited optical resolution is more common [99, 100]. Here, we use DNA origami on mica as a sample which provides AFM topography and allows for the positioning of fluorophores in well defined positions on the origami (Figure 41).

We were able to determine the position of the fluorophores with respect to the geometry of the DNA nanostructure as determined from the topography image, and resolve two fluorophores about 21 nm apart.

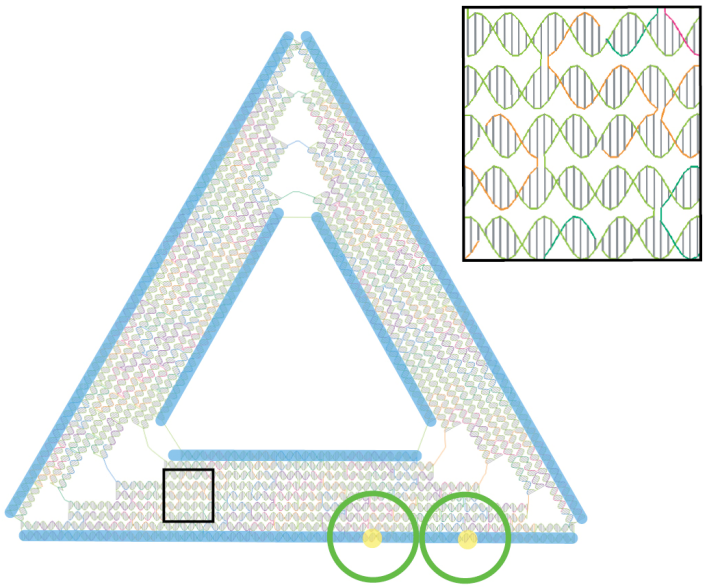

Figure 41

DNA origami triangle structure. The bottom side is 120 nm long. The position of the Atto655 molecules is marked by yellow dots. The structure is outlined in blue and the position of the fluorophores in green, as will be used in Figure 43 and Figure 44.

The fluorescence of Atto655 on mica was less stable than on glass. More blinking and faster bleaching led to a low yield of good scans. The stability of the dyes could be improved noticeably by keeping the air around the sample very dry[14]. The fluorescence intensity of a combined scan (Figure 42) shows the emission of several molecules which exhibit blinking and bleaching. A few quenching spots can be distinguished in the image (green circles in Figure 42). The position of the

[14] A dehumidifier was used to keep the room dry, and silica gel drying pearls were placed around the microscope.

spots was transferred onto the topography image (left). The position of the circles is indeed where it was expected to be on the DNA triangles. Most scans that were taken did not show two well distinguishable quenched spots from one triangle, because they bleached too soon. The topography is not as good as could be expected from a high resolution AFM scan. This is due to vibration that coupled into the system through the microscope objective; it is a common problem in combined AFM/fluorescence microscopy.

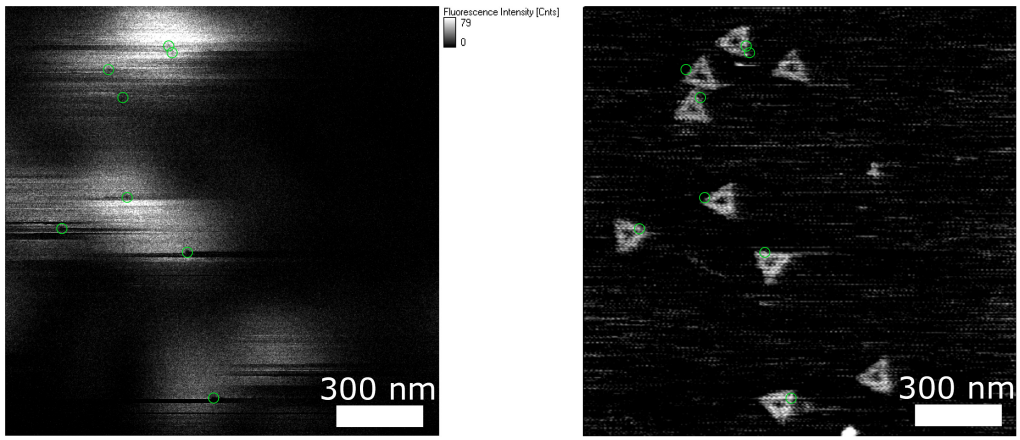

Figure 42

Fluorescence intensity (left) and topography (right) data from a combined scan of DNA origami labeled with two Atto655 molecules

To reduce some of the noise in the scans, the images were Fourier filtered using standard scanning probe microscopy software (section 2.11). Figure 43 shows a combined scan at higher pixel resolution. The structure of the triangle can be clearly seen and even the joint regions in the corners can be made out as holes in the triangle structure. The fluorescence intensity image shows only one quenched spot. One of the molecules bleached after a few scan lines. The known shape of the structure is outlined in the topography image, and transferred to the intensity image to confirm the location of the Atto655 molecule. The outline of the structure is not adapted for size, but rotated to match the topography image and the location of the quenched spot[15].

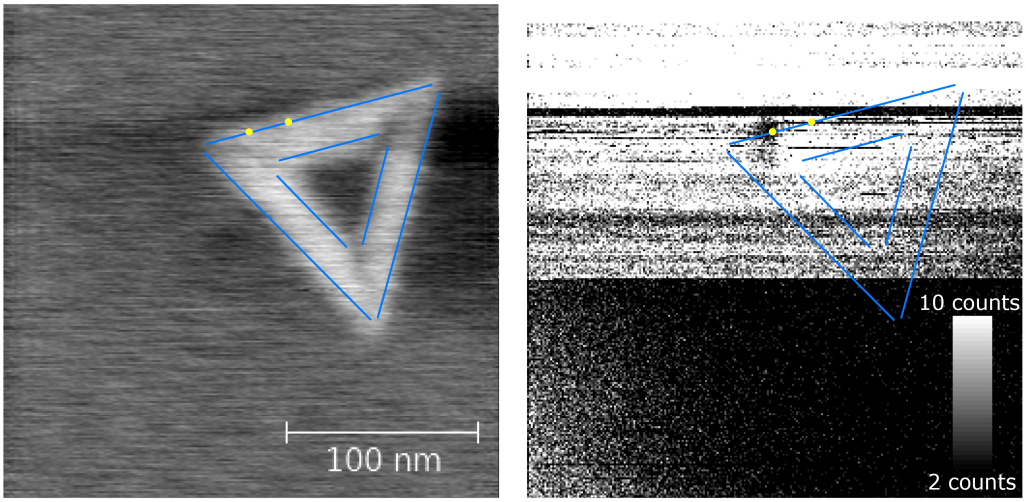

Figure 43

Combined scan at higher pixel resolution.

Several scans were taken where two quenched spots from one DNA triangle could be clearly seen. Figure 44 shows examples of scans with two spots.

[15] At the resolution that could be reached in the topography image, the structure of the DNA origami is essentially rotationally symmetric.

As before, the outline of the structure is overlaid with the topography image and then turned or flipped to match the quenched spots. Flipping is necessary in case the molecule lies “upside-down” (b,c, and d in Figure 44).

From the sections of the scans with two spots, the distance between the Atto655 molecules can be determined. The separation of the dyes was found to be 20.5 +/- 1.55 nm, averaged over eight scan; the error is the standard deviation. Only two scans deviated from this value within the error, which is one pixel or 2.9 nm.

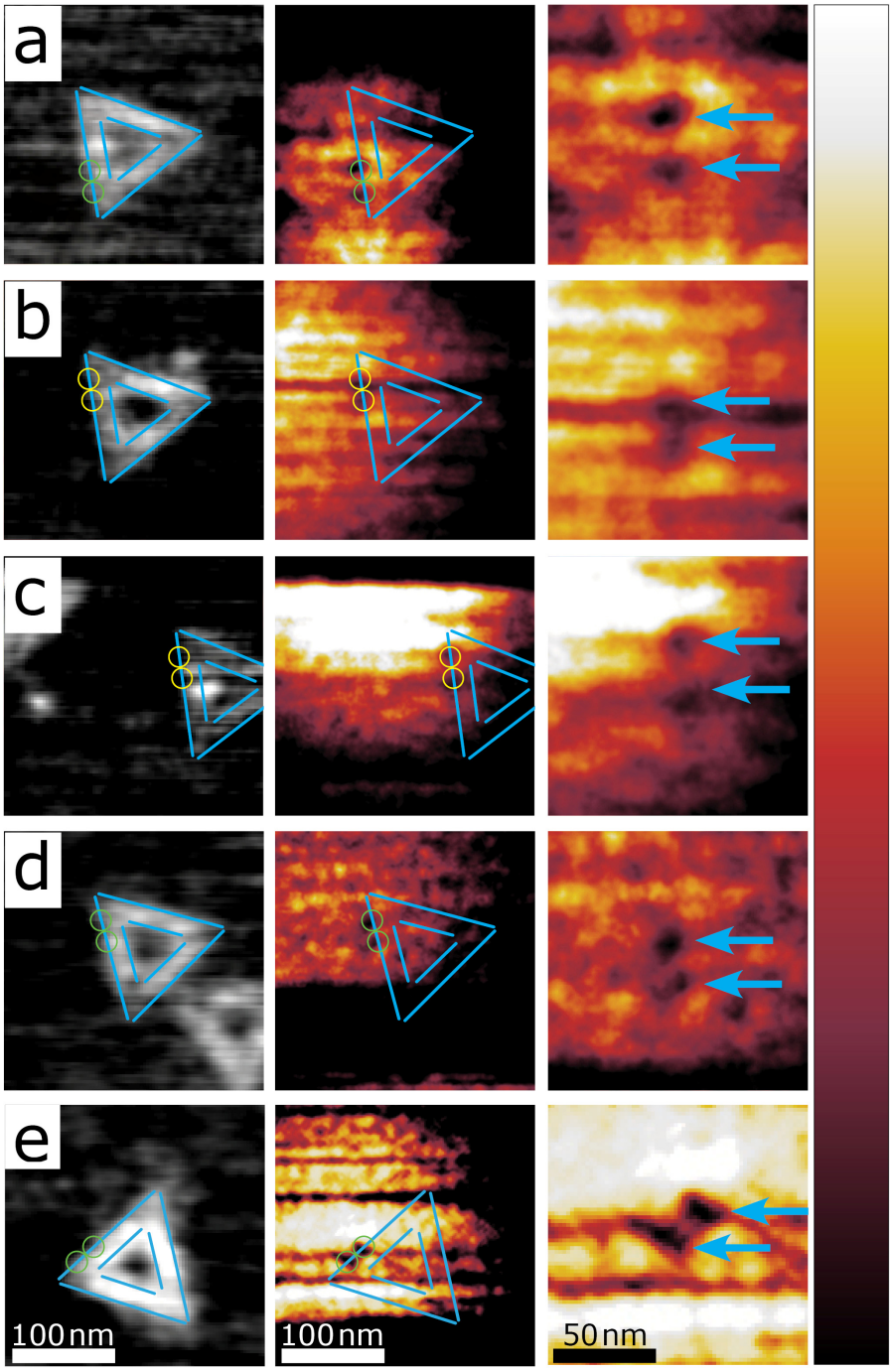

Figure 44

Examples of combined scans that show two quenched spots on one DNA origami triangle. The color scales have been adjusted for best visual contrast. The lowest color value is in general higher than 0 counts.

CHAPTER 4 CONCLUSION

Optical near-field microscopy is an extensively studied field, where the emphasis is mostly on large enhancements of the optical signal by use of materials with electronic resonances near the frequencies of light used, or special geometries which lead to an enhancement of the electric field. Here, we have taken a different path. We have studied materials, which are optically "boring" in the sense that they do not couple strongly to visible light. We found that for three commercially available AFM probe materials, silicon, silicon nitride, and quartz, strong and highly localized quenching of fluorescence of organic fluorophores occurs when the probe is in contact with the molecule. In the case of silicon, the data can be explained with a simple model which calculates the change in fluorescence due to the tip based on classical electrodynamics. In the case of silicon nitride and quartz, the model predicts a reduction of fluorescence under the tip which is lower than what we measured. We found quenching of about 97% efficiency, where the model predicts only 86% and 71% for silicon nitride and quartz for measurements in air. A hypothesis to explain the high efficiency of quenching is the following. As outlined in section 1.2.4, organic molecules change their fluorescence properties when high pressures are applied. Fluorescence at 650 nm would be red-shifted to 686 nm for a pressure increase of 1 GPa. For imaging in air, high adhesive forces can lead to pressures of a few GPa under the tip. For the red fluorophores which were mainly studied in this work

because of their stability, this red shift was not confirmed because the wavelength of emission of these fluorophores is already near the end of the range of detection of our setup. The experiments with a green emitting dye were not successful because blinking and bleaching of fluorescence and autofluorescence from the sample surface interfered with the measurement.

In addition to the measurements in air, we showed that the fluorescence of Atto655 in water is quenched when the AFM probe is in close proximity to the molecule. The data suggests that in the case of quartz probes, the quenched spots are smaller than in air, which promises higher resolutions for imaging in liquid. In one successful combined experiment with a silicon probe, we measured a quenched spot size of 5 nm, which is considerably smaller than what has been achieved in near-field microscopy in liquid so far (15 nm FWHM [82]).

Finally, we employed DNA origami as a sample which provides topography while carrying two fluorophores at defined positions. We were able to resolve the geometry of the DNA structures and localize the fluorophores attached to it. With two Atto655 molecules 21 nm apart on the DNA, we showed true resolution of two fluorophores well beyond the diffraction limit.

Using tip induced quenching in near-field microscopy has the potential to reach very high optical resolutions. For quartz tips in water, where the optical influence of the probe is weak, quenching which is attributed to pressure from the tip dominates. This interaction is very short range, since it requires physical

contact of the tip and the molecule. For very sharp tips, resolutions well below 5 nm can be expected.

REFERENCES

1. G. Binnig, C. F. Quate, and C. Gerber, "Atomic Force Microscope," Phys.Rev.Lett. **56**, 930-933 (1986).

2. B. Bhushan, and Knovel (Firm), "Springer handbook of nanotechnology," (Springer,, Berlin ; New York, 2004), pp. xxxvi, 1222 p.

3. A. Fuhrmann, and R. Ros, "Single-molecule force spectroscopy: a method for quantitative analysis of ligand-receptor interactions," Nanomedicine **5**, 657-666 (2010).

4. S. Kasas, and G. Dietler, "Probing nanomechanical properties from biomolecules to living cells," Pflugers Archiv-European Journal of Physiology **456**, 13-27 (2008).

5. W. E. Moerner, and D. P. Fromm, "Methods of single-molecule fluorescence spectroscopy and microscopy," Review of Scientific Instruments **74**, 3597-3619 (2003).

6. K. Suhling, P. M. W. French, and D. Phillips, "Time-resolved fluorescence microscopy," Photochemical & Photobiological Sciences **4**, 13-22 (2005).

7. P. Tinnefeld, and M. Sauer, "Branching out of single-molecule fluorescence spectroscopy: challenges for chemistry and influence on biology," Angewandte Chemie (International ed. in English) **44**, 2642-2671 (2005).

8. B. Valeur, *Molecular fluorescence : principles and applications* (Wiley-VCH, Weinheim, 2002).

9. M. Sauer, D. Graham, and P. Tinnefeld, "Advanced markers and labels for life science and biomedical applications," Journal of Biophotonics **4**, 375-376 (2011).

10. M. F. Frasco, and N. Chaniotakis, "Bioconjugated quantum dots as fluorescent probes for bioanalytical applications," Analytical and Bioanalytical Chemistry **396**, 229-240 (2010).

11. X. Wang, X. Ren, K. Kahen, M. a. Hahn, M. Rajeswaran, S. Maccagnano-Zacher, J. Silcox, G. E. Cragg, A. L. Efros, and T. D. Krauss, "Non-blinking semiconductor nanocrystals," Nature **459**, 686-689 (2009).

12. P. Tinnefeld, V. Buschmann, D.-P. Herten, K.-T. Han, and M. Sauer, "Confocal Fluorescence Lifetime Imaging Microscopy (FLIM) at the Single

Molecule Level," Single Molecules **1**, 215-223 (2000).

13. C. M. Pieper, and J. Enderlein, "Fluorescence correlation spectroscopy as a tool for measuring the rotational diffusion of macromolecules," Chemical Physics Letters **516**, 1-11 (2011).

14. M. J. Rust, M. Bates, and X. W. Zhuang, "Sub-diffraction-limit imaging by stochastic optical reconstruction microscopy (STORM)," Nature Methods **3**, 793-795 (2006).

15. T. Dertinger, R. Colyer, G. Iyer, S. Weiss, and J. Enderlein, "Fast, background-free, 3D super-resolution optical fluctuation imaging (SOFI)," Proceedings of the National Academy of Sciences of the United States of America **106**, 22287-22292 (2009).

16. J. Vogelsang, R. Kasper, C. Steinhauer, B. Person, M. Heilemann, M. Sauer, and P. Tinnefeld, "A reducing and oxidizing system minimizes photobleaching and blinking of fluorescent dyes," Angewandte Chemie-International Edition **47**, 5465-5469 (2008).

17. E. A. J. Reits, and J. J. Neefjes, "From fixed to FRAP: measuring protein mobility and activity in living cells," Nature Cell Biology **3**, E145-E147 (2001).

18. B. Valeur, and I. Leray, "Design principles of fluorescent molecular sensors for cation recognition," Coordination Chemistry Reviews **205**, 3-40 (2000).

19. I. Rasnik, S. A. McKinney, and T. Ha, "Nonblinking and longlasting single-molecule fluorescence imaging," Nature Methods **3**, 891-893 (2006).

20. J. Widengren, A. Chmyrov, C. Eggeling, P.-A. Loefdahl, and C. A. M. Seidel, "Strategies to improve photostabilities in ultrasensitive fluorescence spectroscopy," Journal of Physical Chemistry A **111**, 429-440 (2007).

21. T. Ha, "Single-molecule fluorescence resonance energy transfer," Methods **25**, 78-86 (2001).

22. J. Enderlein, "Electrodynamics of Fluorescence," (2003), http://www.joerg-enderlein.de/fileadmin/downloads/Tutorial.pdf, Accessed Feb 22nd, 2012.

23. T. Forster, "Zwischenmolekulare Energiewanderung und Fluoreszenz," Annalen Der Physik **2**, 55-75 (1948).

24. D. L. Dexter, "A Theory of Sensitized Luminescence in Solids," Journal of

Chemical Physics **21**, 836-850 (1953).

25. P. F. Jones, "Spectral Shifts and Broadening of Fluorescence of Anthracene and Tetracence in Several Host Crystals at High Pressures," Journal of Chemical Physics **48**, 5448-& (1968).

26. D. S. McClure, "Dispersion Forces in Molecular Crystals," in *Symposium on Electrical Conductivity in Organic Solids*, H. Kallmann, and M. Silver, eds. (Wiley Interscience, Duke University, Durham, North Carolina, 1960), pp. 219-238.

27. M. Croci, H. J. Muschenborn, F. Guttler, A. Renn, and U. P. Wild, "Single-Molecule Spectroscopy - Pressure Effect on Pentacene in P-Terphenyl," Chemical Physics Letters **212**, 71-77 (1993).

28. P. F. Jones, and M. Nicol, "Excimer Emission of Naphtalene Anthracence and Phenanthrene Crystals Produced by Very High Pressures," Journal of Chemical Physics **48**, 5440-& (1968).

29. P. F. Jones, and M. Nicol, "Fluorescence of Doped Crystals of Anthracence Naphtalene and Phenantrene Under High Pressures - Role of Excimers in Energy Transfer to Guest Molecules," Journal of Chemical Physics **48**, 5457-& (1968).

30. B. Huang, M. Bates, and X. Zhuang, "Super-resolution fluorescence microscopy," Annual review of biochemistry **78**, 993-1016 (2009).

31. S. W. Hell, "Far-field optical nanoscopy," Science **316**, 1153-1158 (2007).

32. S. W. Hell, and J. Wichmann, "Breaking the diffraction resolution limit by stimulated emission: stimulated-emission-depletion fluorescence microscopy," Optics letters **19**, 780-782 (1994).

33. B. Hein, K. I. Willig, and S. W. Hell, "Stimulated emission depletion (STED) nanoscopy of a fluorescent protein-labeled organelle inside a living cell," Proceedings of the National Academy of Sciences of the United States of America **105**, 14271-14276 (2008).

34. A. Pertsinidis, Y. Zhang, and S. Chu, "Subnanometre single-molecule localization, registration and distance measurements," Nature **466**, 647-U611 (2010).

35. A. Yildiz, and P. R. Selvin, "Fluorescence imaging with one nanometer accuracy: application to molecular motors," Accounts of chemical research **38**, 574-582 (2005).

36. R. E. Thompson, D. R. Larson, and W. W. Webb, "Precise nanometer localization analysis for individual fluorescent probes," Biophysical Journal **82**, 2775-2783 (2002).

37. E. Betzig, G. H. Patterson, R. Sougrat, O. W. Lindwasser, S. Olenych, J. S. Bonifacino, M. W. Davidson, J. Lippincott-Schwartz, and H. F. Hess, "Imaging intracellular fluorescent proteins at nanometer resolution," Science **313**, 1642-1645 (2006).

38. T. Klein, A. Loschberger, S. Proppert, S. Wolter, S. V. van de Linde, and M. Sauer, "Live-cell dSTORM with SNAP-tag fusion proteins," Nature Methods **8**, 7-9 (2011).

39. T. Dertinger, R. Colyer, R. Vogel, J. Enderlein, and S. Weiss, "Achieving increased resolution and more pixels with Superresolution Optical Fluctuation Imaging (SOFI)," Optics express **18**, 18875-18885 (2010).

40. K. H. Drexhage, "Monomolecular Layers and Light," Scientific American **222**, 108-& (1970).

41. R. R. Chance, A. Prock, and R. Silbey, "Molecular fluorescence and energy transfer near interfaces," in *Advances in Chemical Physics*, I. Prigogine, and S. A. Rice, eds. (John Wiley & Sons, Inc., 1978), pp. 1-65.

42. T. Hayashi, T. G. Castner, and R. W. Boyd, "Quenching of Molecular Fluorescence Near the Surface of a Semiconductor," Chemical Physics Letters **94**, 461-466 (1983).

43. M. Brandstatter, P. Fromherz, and A. Offenhausser, "Fluorescent Dye Monolayers on Oxidized Silicon," Thin Solid Films **160**, 341-346 (1988).

44. a. P. Alivisatos, M. F. Arndt, S. Efrima, D. H. Waldeck, and C. B. Harris, "Electronic energy transfer at semiconductor interfaces. I. Energy transfer from two-dimensional molecular films to Si(111)," The Journal of Chemical Physics **86**, 6540-6540 (1987).

45. P. M. Whitmore, A. P. Alivisatos, and C. B. Harris, "Distance Dependence of Electronic-Energy Transfer to Semiconductor Surfaces - 3N-Pi-Star Pyrazine/GaAs(110)," Physical Review Letters **50**, 1092-1094 (1983).

46. L. Danos, R. Greef, and T. Markvart, "Efficient fluorescence quenching near crystalline silicon from Langmuir-Blodgett dye films," Thin Solid Films **516**, 7251-7255 (2008).

47. L. Danos, and T. Markvart, "Excitation energy transfer rate from Langmuir

Blodgett (LB) dye monolayers to silicon: Effect of aggregate formation," Chemical Physics Letters **490**, 194-199 (2010).

48. M. I. Sluch, A. G. Vitukhnovsky, and M. C. Petty, "Anomalous Distance Dependence of Fluorescence Lifetime Quenched by a Semiconductor," Physics Letters A **200**, 61-64 (1995).

49. R. J. Deri, "Interference Effects on the Photo-Luminescence Intensity of Molecules Near a Dielectric Surface," Chemical Physics Letters **98**, 485-490 (1983).

50. W. L. Barnes, "Fluorescence near interfaces: the role of photonic mode density," Journal of Modern Optics **45**, 661-699 (1998).

51. L. Novotny, and S. J. Stranick, "Near-field optical microscopy and spectroscopy with pointed probes," Annual Review of Physical Chemistry **57**, 303-331 (2006).

52. A. Hartschuh, "Tip-Enhanced Near-Field Optical Microscopy," Angewandte Chemie-International Edition **47**, 8178-8191 (2008).

53. R. C. Dunn, "Near-field scanning optical microscopy," Chemical Reviews **99**, 2891-+ (1999).

54. T. J. Yang, G. A. Lessard, and S. R. Quake, "An apertureless near-field microscope for fluorescence imaging," Applied Physics Letters **76**, 378-380 (2000).

55. A. G. T. Ruiter, K. O. van der Werf, J. A. Veerman, M. F. Garcia-Parajo, W. H. J. Rensen, and N. F. van Hulst, "Tuning fork shear-force feedback," Ultramicroscopy **71**, 149-157 (1998).

56. C. Hoppener, R. Beams, and L. Novotny, "Background Suppression in Near-Field Optical Imaging," Nano Letters **9**, 903-908 (2009).

57. E. H. Synge, "A suggested method for extending microscopic resolution into the ultra-microscopic region," PHILOSOPHICAL MAGAZINE **6**, 356 (1928).

58. D. W. Pohl, W. Denk, and M. Lanz, "Optical spectroscopy: Image recording with resolution λ/20," Applied Physics Letters **44**, 651-653 (1984).

59. A. Lewis, M. Isaacson, A. Harootunian, and A. Muray, "Development of a 500 Å spatial resolution light microscope. I. Light is efficiently transmitted through λ/16 diameter apertures," Ultramicroscopy **13**, 227-231 (1984).

60. H. G. Frey, S. Witt, K. Felderer, and R. Guckenberger, "High-resolution imaging of single fluorescent molecules with the optical near-field of a metal tip," Physical Review Letters **93** (2004).

61. C. W. Hollars, and R. C. Dunn, "Probing single molecule orientations in model lipid membranes with near-field scanning optical microscopy," Journal of Chemical Physics **112**, 7822-7830 (2000).

62. C. Hoppener, D. Molenda, H. Fuchs, and A. Naber, "Scanning near-field optical microscopy of a cell membrane in liquid," Journal of Microscopy-Oxford **210**, 288-293 (2003).

63. H. G. Frey, F. Keilmann, A. Kriele, and R. Guckenberger, "Enhancing the resolution of scanning near-field optical microscopy by a metal tip grown on an aperture probe," Applied Physics Letters **81**, 5030-5032 (2002).

64. T. H. Taminiau, F. D. Stefani, F. B. Segerink, and N. F. van Hulst, "Optical antennas direct single-molecule emission," Nature Photonics **2**, 234-237 (2008).

65. Y. Ebenstein, E. Yoskovitz, R. Costi, A. Aharoni, and U. Banin, "Interaction of scanning probes with semiconductor nanocrystals; physical mechanism and basis for near-field optical imaging," Journal of Physical Chemistry A **110**, 8297-8303 (2006).

66. E. Yoskovitz, D. Oron, I. Shweky, and U. Banin, "Apertureless Near-Field Distance-Dependent Lifetime Imaging and Spectroscopy of Semiconductor Nanocrystals," Journal of Physical Chemistry C **112**, 16306-16311 (2008).

67. E. Yoskovitz, G. Menagen, A. Sitt, E. Lachman, and U. Banin, "Nanoscale Near-Field Imaging of Excitons in Single Heterostructured Nanorods," Nano Letters **10**, 3068-3072 (2010).

68. J. M. Gerton, L. A. Wade, G. A. Lessard, Z. Ma, and S. R. Quake, "Tip-enhanced fluorescence microscopy at 10 nanometer resolution," Physical Review Letters **93**, 180801 (2004).

69. B. Sick, B. Hecht, U. P. Wild, and L. Novotny, "Probing confined fields with single molecules and vice versa," Journal of microscopy **202**, 365-373 (2001).

70. Z. Y. Ma, J. M. Gerton, L. A. Wade, and S. R. Quake, "Fluorescence near-field microscopy of DNA at sub-10 nm resolution," Physical Review Letters **97** (2006).

71. C. A. Xie, C. Mu, J. R. Cox, and J. M. Gerton, "Tip-enhanced fluorescence

microscopy of high-density samples," Applied Physics Letters **89** (2006).

72. B. D. Mangum, C. Mu, and J. M. Gerton, "Resolving single fluorophores within dense ensembles: contrast limits of tip-enhanced fluorescence microscopy," Optics Express **16**, 6183-6193 (2008).

73. C. Mu, B. D. Mangum, C. Xie, and J. M. Gerton, "Nanoscale fluorescence microscopy using carbon nanotubes," Ieee Journal of Selected Topics in Quantum Electronics **14**, 206-216 (2008).

74. W. Trabesinger, A. Kramer, M. Kreiter, B. Hecht, and U. P. Wild, "Single-molecule near-field optical energy transfer microscopy," Applied Physics Letters **81**, 2118-2120 (2002).

75. A. Kramer, W. Trabesinger, B. Hecht, and U. P. Wild, "Optical near-field enhancement at a metal tip probed by a single fluorophore," Applied Physics Letters **80**, 1652-1654 (2002).

76. J. N. Farahani, H.-J. Eisler, D. W. Pohl, M. Pavius, P. Flueckiger, P. Gasser, and B. Hecht, "Bow-tie optical antenna probes for single-emitter scanning near-field optical microscopy," Nanotechnology **18** (2007).

77. A. Kinkhabwala, Z. F. Yu, S. H. Fan, Y. Avlasevich, K. Mullen, and W. E. Moerner, "Large single-molecule fluorescence enhancements produced by a bowtie nanoantenna," Nature Photonics **3**, 654-657 (2009).

78. S. Kühn, U. Håkanson, L. Rogobete, and V. Sandoghdar, "Enhancement of Single-Molecule Fluorescence Using a Gold Nanoparticle as an Optical Nanoantenna," Physical Review Letters **97**, 1-4 (2006).

79. P. Das, and A. Puri, "Energy flow and fluorescence near a small metal particle," Physical Review B **65**, 1-8 (2002).

80. C. Hoppener, and L. Novotny, "Antenna-based optical imaging of single Ca2+ transmembrane proteins in liquids," Nano Letters **8**, 642-646 (2008).

81. C. Hoppener, and L. Novotny, "Imaging of membrane proteins using antenna-based optical microscopy," Nanotechnology **19** (2008).

82. H. G. Frey, J. Paskarbeit, and D. Anselmetti, "Tip-enhanced single molecule fluorescence near-field microscopy in aqueous environment," Applied Physics Letters **94** (2009).

83. J. Azoulay, A. Debarre, A. Richard, and P. Tchenio, "Quenching and enhancement of single-molecule fluorescence under metallic and dielectric tips,"

Europhysics Letters **51**, 374-380 (2000).

84. M. Sukharev, and T. Seideman, "Optical Properties of Metal Tips for Tip-Enhanced Spectroscopies," Journal of Physical Chemistry A **113**, 7508-7513 (2009).

85. E. Moreno, D. Erni, C. Hafner, and R. Vahldieck, "Multiple multipole method with automatic multipole setting applied to the simulation of surface plasmons in metallic nanostructures," Journal of the Optical Society of America a-Optics Image Science and Vision **19**, 101-111 (2002).

86. P. Bharadwaj, and L. Novotny, "Spectral dependence of single molecule fluorescence enhancement," Optics Express **15**, 14266-14274 ST - Spectral dependence of single mo (2007).

87. Q. Li, J. Zheng, and Z. Liu, "Site-Selective Assemblies of Gold Nanoparticles on an AFM Tip-Defined Silicon Template," Langmuir **19**, 166-171 (2003).

88. J. W. Zheng, Z. H. Zhu, H. F. Chen, and Z. F. Liu, "Nanopatterned assembling of colloidal gold nanoparticles on silicon," Langmuir **16**, 4409-4412 (2000).

89. H. Cheng, K. Zhang, J. A. Libera, M. O. de la Cruz, and M. J. Bedzyk, "Polynucleotide adsorption to negatively charged surfaces in divalent salt solutions," Biophysical Journal **90**, 1164-1174 (2006).

90. P. W. K. Rothemund, "Folding DNA to create nanoscale shapes and patterns," Nature **440**, 297-302 (2006).

91. D. Patra, I. Gregor, and J. Enderlein, "Image analysis of defocused single-molecule images for three-dimensional molecule orientation studies," Journal of Physical Chemistry A **108**, 6836-6841 (2004).

92. G. D. Marshall, T. Gaebel, J. C. F. Matthews, J. Enderlein, J. L. O'Brien, and J. R. Rabeau, "Coherence properties of a single dipole emitter in diamond," New Journal of Physics **13**, 055016 (2011).

93. M. A. Green, and M. J. Keevers, "OPTICAL-PROPERTIES OF INTRINSIC SILICON AT 300 K," Progress in Photovoltaics **3**, 189-192 (1995).

94. T. Baak, "Silicon Oxynitride - A Material for GRIN Optics," Applied Optics **21**, 1069-1072 (1982).

95. S. Balme, J.-M. Janot, P. Dejardin, E. N. Vasina, and P. Seta,

"Potentialities of confocal fluorescence for investigating protein adsorption on mica and in ultrafiltration membranes," Journal of Membrane Science **284**, 198-204 (2006).

96. A. Benda, V. Fagul'ova, A. Deyneka, J. Enderlein, and M. Hof, "Fluorescence lifetime correlation spectroscopy combined with lifetime tuning: New perspectives in supported phospholipid bilayer research," Langmuir **22**, 9580-9585 (2006).

97. W. Trabesinger, a. Kramer, M. Kreiter, B. Hecht, and U. P. Wild, "Single-molecule near-field optical energy transfer microscopy with dielectric tips," Journal of microscopy **209**, 249-253 (2003).

98. F. R. Aussenegg, A. Leitner, M. E. Lippitsch, H. Reinisch, and M. Riegler, "Novel Aspects of Fluorescence Lifetime for Molecules Positioned Close to Metal-Surfaces," Surface Science **189**, 935-945 (1987).

99. A. Noy, and T. R. Huser, "Combined force and photonic probe microscope with single, molecule sensitivity," Review of Scientific Instruments **74**, 1217-1221 (2003).

100. Y. Ebenstein, N. Gassman, S. Kim, and S. Weiss, "Combining atomic force and fluorescence microscopy for analysis of quantum-dot labeled protein-DNA complexes," Journal of Molecular Recognition **22**, 397-402 (2009).